HHS Public Access

Author manuscript

Cancer Discov. Author manuscript; available in PMC 2020 July 01.

Published in final edited form as:

Cancer Discov. 2020 January ; 10(1): 104–123. doi:10.1158/2159-8290.CD-19-1006.

Atypical KRAS^{G12R} Mutant Is Impaired in PI3K Signaling and Macropinocytosis in Pancreatic Cancer

G. Aaron Hobbs[1], **Nicole M. Baker**[1], **Anne M. Miermont**[2], **Ryan D. Thurman**[3], **Mariaelena Pierobon**[4], **Timothy H. Tran**[5], **Andrew O. Anderson**[2], **Andrew M. Waters**[6], **J. Nathaniel Diehl**[7], **Bjoern Papke**[6], **Richard G. Hodge**[6], **Jennifer E. Klomp**[6], **Craig M. Goodwin**[6], **Jonathan M. DeLiberty**[1], **Junning Wang**[8], **Raymond W. S. Ng**[8], **Prson Gautam**[9], **Kirsten L. Bryant**[1], **Dominic Esposito**[5], **Sharon L. Campbell**[3,6], **Emanuel F. Petricoin III**[4], **Dhirendra K. Simanshu**[5], **Andrew J. Aguirre**[8,10], **Brian M. Wolpin**[8], **Krister Wennerberg**[9,11], **Udo Rudloff**[2,12], **Adrienne D. Cox**[1,6,13], **Channing J. Der**[1,6,7]

[1]Department of Pharmacology, University of North Carolina at Chapel Hill, Chapel Hill, North Carolina. [2]Thoracic & GI Oncology Branch, National Cancer Institute. Bethesda, Maryland. [3]Department of Biochemistry and Biophysics, University of North Carolina at Chapel Hill, Chapel Hill, North Carolina. [4]Center for Applied Proteomics and Molecular Medicine, George Mason University, Manassas, Virginia. [5]NCI RAS Initiative, Cancer Research Technology Program, Frederick National Laboratory for Cancer Research, Leidos Biomedical Research, Inc., Frederick, Maryland. [6]Lineberger Comprehensive Cancer Center, University of North Carolina at Chapel Hill, Chapel Hill, North Carolina. [7]Curriculum in Genetics and Molecular Biology, University of North Carolina at Chapel Hill, Chapel Hill, North Carolina. [8]Department of Medical Oncology, Dana-Farber Cancer Institute, Boston, Massachusetts. [9]Institute for Molecular Medicine Finland (FIMM), University of Helsinki, Helsinki, Finland. [10]Broad Institute of MIT and Harvard, Cambridge, Massachusetts. [11]Biotech Research & Innovation Centre (BRIC), University of Copenhagen, Copenhagen, Denmark. [12]Rare Tumor Initiative, Pediatric Oncology Branch, National Cancer Institute, Bethesda, MD [13]Department of Radiation Oncology, University of North Carolina at Chapel Hill, Chapel Hill, North Carolina.

Corresponding authors: Channing J. Der, Lineberger Comprehensive Cancer Center, University of North Carolina at Chapel Hill, Chapel Hill, NC 27514. Phone: 919-966-5634; cjder@med.unc.edu; and Udo Rudloff, Center for Cancer Research, National Cancer Institute, Building 10 - Hatfield CRC, Room 2B-34D, Bethesda, MD 20892; Phone: 240-760-6238; rudloffu@mail.nih.gov.

Author's Contributions

Conception and design: G.A. Hobbs, U. Rudloff and C.J. Der

Development of methodology: G.A. Hobbs, N.M. Baker, M. Pierobon, B. Papke, U. Rudloff, C.J. Der

Acquisition of data (provided animals, acquired and managed patients, provided facilities, etc.): G.A. Hobbs, N.M. Baker, A.M. Miermont, R.D. Thurman, M. Pierobon, T.H. Tran, A. Anderson, A.M. Waters, J.N. Diehl, B. Papke, R.G. Hodge, J. M. DeLiberty, K.L. Bryant, J. Wang, R. Ng, P. Gautam, D. Esposito, D.K. Simanshu, B.M. Wolpin, A.J. Aguirre

Analysis and interpretation of data (e.g. statistical analysis, biostatistics, computational analysis): G.A. Hobbs, M. Pierobon, J.E. Klomp, C.M. Goodwin, J. M. DeLiberty, J. Wang, R. Ng, P. Gautam, S.L. Campbell, E.F. Petricoin, III, D.K. Simanshu, U. Rudloff, A.J. Aguirre, A.D. Cox, C.J. Der

Writing, review, and/or revision of the manuscript: G.A. Hobbs, A.D. Cox, C.J. Der

Administration, technical, or material support (i.e., reporting or organizing data, constructing databases): G.A. Hobbs, M. Pierobon, J.E. Klomp, C.M. Goodwin, A.D. Cox, C.J. Der

Study supervision: U. Rudloff, A.D. Cox, C.J. Der

Data and Materials Availability: The atomic coordinates and structure factors for the crystal structure of GMPPNP-bound KRAS^{G12R} have been deposited in the Protein Data Bank under accession code 6CU6.The datasets generated for the current study are available from the corresponding authors upon request.

Abstract

Allele-specific signaling by different KRAS alleles remains poorly understood. The *KRAS*^{G12R} mutation displays uneven prevalence among cancers that harbor the highest occurrence of *KRAS* mutations: it is rare in lung and colorectal cancers (~1%), yet relatively common (~20%) in pancreatic ductal adenocarcinoma (PDAC), suggesting context-specific properties. We evaluated whether KRAS^{G12R} is functionally distinct from the more common KRAS^{G12D} or KRAS^{G12V} mutant proteins (KRAS$^{G12D/V}$). We found that KRAS$^{G12D/V}$ but not KRAS^{G12R} drives macropinocytosis and that MYC is essential for macropinocytosis in KRAS$^{G12D/V}$ but not KRAS^{G12R}-mutant PDAC. Surprisingly, we found that KRAS^{G12R} is defective for interaction with a key effector, p110α phosphoinositide 3-kinase (PI3Kα), due to structural perturbations in switch II. Instead, upregulated KRAS-independent PI3Kγ activity was able to support macropinocytosis in KRAS^{G12R}-mutant PDAC. Finally, we determined that KRAS^{G12R}-mutant PDAC displayed a distinct drug sensitivity profile compared with KRAS^{G12D}-mutant PDAC but is still responsive to the combined inhibition of ERK and autophagy.

INTRODUCTION

Mutational activation of the *KRAS* oncogene is the predominant oncogenic alteration in the top three major cancers (lung, colorectal and pancreatic), ranked by mortality, in the US (1). Thus, effective anti-KRAS therapeutic strategies are expected to make a significant impact on cancer treatment. To date, there are no effective pan-KRAS mutant therapies (2). However, with inhibitors specifically targeting the glycine-to-cysteine (G12C) missense mutation now entering clinical evaluation (3), an emerging premise is that KRAS mutation-selective therapies may be feasible (4). Cancer-associated mutations in KRAS cluster in one of three hotspots, with a majority (84%) of mutations causing single amino acid substitutions at G12 (1). Of the six possible single-base missense mutations that can occur at G12, G12D is the most predominant (42%), followed by G12V, G12C, G12A, G12S and G12R, the last of which occurs infrequently in most cancers.

However, while the *KRAS*^{G12R} mutation is rare in lung and colorectal cancers (~1%), it is the third most common *KRAS* mutation in PDAC (5). Recent TCGA analyses of PDAC suggested that *KRAS*^{G12R}-mutant cancers can harbor additional *KRAS* mutations, implying that KRAS^{G12R} may be functionally distinct from other *KRAS* driver mutations (6). Unexpectedly, we found that KRAS^{G12R} fails to bind the PI3K catalytic subunit p110α, an essential effector for KRAS-driven cancer initiation and maintenance (7), resulting in KRAS-independent macropinocytosis, a nutrient uptake process that has been shown to be necessary for PDAC tumor growth (8). Using x-ray crystallography, we found that KRAS^{G12R}, unlike KRAS^{G12D}, disrupts the switch II (SII) region critical for effector interaction. Instead, KRAS-independent p110γ PI3K activity supports macropinocytosis in KRAS^{G12R}-mutant PDAC. Finally, we addressed the possibility that KRAS^{G12R}- and KRAS^{G12D}-mutant PDAC may exhibit distinct therapeutic vulnerabilities. KRAS^{G12R}-mutant PDAC showed limited preferential sensitivity to MEK/ERK inhibitor monotherapy, with only a modest difference in comparison to PDAC models harboring the more common KRAS$^{G12D/V}$ mutants. However, using drug sensitivity resistance testing (DSRT) to probe 525 different inhibitors, we observed that KRAS^{G12R}-mutant PDAC was also sensitive to

autophagy inhibitors. We found that the recently reported combination of ERK MAPK inhibition and the autophagy inhibitor chloroquine can be a rapidly translatable, effective therapeutic strategy for patients harboring these mutations. Thus, we have demonstrated structurally and functionally distinct properties for $KRAS^{G12R}$ that lead to alternative activation of macropinocytosis through PI3Kγ and enhanced sensitivity to combined ERK MAPK pathway and autophagy inhibition.

RESULTS

$KRAS^{G12R}$-Independent Macropinocytosis

Despite its status as the third most prevalent *KRAS* mutation in PDAC, after G12D and G12V (Supplementary Fig. S1A), $KRAS^{G12R}$ has been poorly studied. Given the role of oncogenic KRAS in altering metabolic activities to support cancer growth (9), we first sought to determine if $KRAS^{G12R}$ plays a role similar to the more common KRAS mutants in driving metabolic perturbations. Accordingly, we examined macropinocytosis, a nutrient-scavenging process shown to sustain PDAC tumor growth (10). Upon quantifying macropinocytosis activity by uptake of fluorescein isothiocyanate (FITC)-tagged dextran, we detected variable levels of macropinocytosis in our panel of 10 *KRAS*-mutant PDAC cell lines (Fig. 1A). In agreement with Bar-Sagi and colleagues (10), transient siRNA suppression of *KRAS* reduced macropinocytosis in *KRAS* G12D-, G12V- and G12C-mutant cell lines (Figs. 1B–D). Surprisingly, suppression of *KRAS* did not reduce macropinocytosis in the $KRAS^{G12R}$-mutant PDAC lines (Figs. 1B–D), indicating that they displayed KRAS-independent macropinocytosis. This unexpected finding raised the possibility that the growth of $KRAS^{G12R}$-mutant PDAC may also be KRAS independent. However, as we have described previously for $KRAS^{G12D/V/C}$-mutant PDAC cell lines (11), we observed that both anchorage-dependent and -independent *in vitro* growth of the $KRAS^{G12R}$-mutant cell lines were also KRAS dependent (Fig. 1E and F). Further, loss of each KRAS mutant was associated with increased apoptosis and impaired cell cycle progression (Supplementary Fig. S1B and S1C).

We applied two strategies to determine if $KRAS^{G12R}$ could stimulate macropinocytosis in other cellular contexts. First, we ectopically expressed different KRAS mutants in three cell models sensitive to mutant KRAS-driven growth transformation (12,13) and quantified macropinocytosis by FITC-dextran uptake. Stable expression of G12D or G12V, but not G12R, increased macropinocytosis in RIE-1 rat intestinal epithelial cells (Figs. 2A–C) in a time-dependent manner (Supplementary Fig. S2A and S2B). Similar results were observed in NIH/3T3 mouse fibroblasts (Supplementary Figs. S2C–E) and hTERT-immortalized HPNE human pancreatic duct-derived epithelial cells (Supplementary Figs. S2F–H).

We also assessed macropinocytosis using BODIPY-conjugated bovine serum albumin (DQ-BSA), which has a fluorescent signal that is quenched until it is released upon proteolytic degradation following macropinosome fusion with lysosomes (10). Concordant with the results obtained with FITC-dextran, stable expression of $KRAS^{G12D/V}$ stimulated macropinocytosis relative to empty vector and $KRAS^{G12R}$ in RIE-1 cells (Fig. 2D). Thus, while $KRAS^{G12R}$ could cause the same morphologic transformation of RIE-1 cells as

KRAS$^{G12D/V}$ (Supplementary Fig. S2I), KRAS^{G12R} uniquely failed to stimulate macropinocytosis.

Our second strategy was to determine whether exogenous KRAS^{G12R} could rescue macropinocytosis in siRNA-suppressed *KRAS*$^{G12D/V}$-mutant PDAC cell lines. However, exogenous expression of mutant KRAS in KRAS-mutant PDAC cells is growth inhibitory, and stable suppression of endogenous mutant KRAS can lead to confounding compensatory activities (14). To overcome these technical issues, we used a doxycycline-inducible expression vector to transiently express exogenous mutant KRAS^{G12R} concurrently with *KRAS* siRNA oligo treatment to transiently silence endogenous *KRAS*^{G12D} in AsPC-1 cells (Figs. 2E–G) and *KRAS*^{G12V} in Pa04C cells (Figs. 2H–J). Ectopic expression that restored the same mutant as endogenous KRAS was able to rescue macropinocytosis, whereas ectopic expression of KRAS^{G12R} failed to restore KRAS$^{G12D/V}$-dependent PDAC macropinocytosis.

KRAS^{G12R} Uniquely Alters the Structure of Switch II

Previously, KRAS^{G12R} has been reported to have decreased intrinsic GTPase activity and be insensitive to GAP-mediated hydrolysis, similar to other KRAS G12 mutants (15,16). However, sensitivity to GEFs had been unexplored. As Son of Sevenless (SOS1) is considered the main RASGEF, we measured the k_{cat} of exchange with KRAS^{WT} and G12 mutants using the catalytic domain of SOS1 (SOS^{cat}). Similar to what has been described for HRAS^{G12V} (17), we found that SOS^{cat} activity towards KRAS^{G12V} was reduced 20% (0.01653 $\mu M^{-1}s^{-1}$) and 60% towards KRAS^{G12D} (0.007982 $\mu M^{-1}s^{-1}$) compared with KRAS^{WT} (0.01986 $\mu M^{-1}s^{-1}$). In contrast, SOS^{cat} was inactive towards KRAS^{G12R} (Fig. 3A). To determine if this impaired activity was due to loss of allosteric interaction or catalysis, we evaluated the activity of the CDC25 catalytic fragment of a different RASGEF, RASGRP1. Although its CDC25 domain has a similar catalytic mechanism as the SOS1 CDC25 domain, the RASGRP1 REM-CDC25 catalytic fragment (RASGRP1^{cat}) lacks the requirement for allosteric-mediated RAS activation (18). KRAS^{G12R} was activated equivalently to KRAS^{WT} by RASGRP1^{cat} (Fig. 3B), indicating that KRAS^{G12R} fails to interact with the allosteric binding site of SOS1.

As the loss of binding to the allosteric domain of SOS^{cat} suggested a large structural change in KRAS^{G12R}, we determined the structure of human KRAS4B^{G12R} (residues 1–169) bound to the GTP analog GMPPNP at a resolution of 1.5 Å (Fig. 3C; Table S1). Both switch I (SI; residues 30–40) and switch II (SII; residues 60–76) undergo conformational changes during RAS GDP-GTP cycling and are critical for interaction with effectors and regulators (19). In the structure of GMPPNP-bound KRAS^{G12R}, SI is in the same conformation as in GMPPNP-bound RAS^{WT}. However, in KRAS^{G12R}, helix α2 in SII is partially unfolded and contains only one helical turn instead of four. The G12R mutation alters SII by displacing Q61 and forming a direct interaction with E62 and T35, a residue that interacts with the Mg^{2+} ion and γ-phosphate in the GTP-bound state (Fig. 3D). An overlay of the crystal structures of GMPPNP-bound KRAS^{G12R} and KRAS^{G12D} (20) shows the distinct structural alterations in SII induced by the G12R mutation (Figs. 3E and F).

The distribution of specific G12 mutations differs across RAS isoforms (COSMIC v89). For example, G12V represents 50% of all HRAS G12 mutations, whereas G12D is much less common in HRAS than in KRAS (18% vs 42%), and G12R represents just 3% of all HRAS G12 mutations in cancer. Thus, we wondered whether specific mutations may have isoform-specific consequences. Comparison with a structure of GMPPNP-bound $HRAS^{G12V}$ (Supplementary Fig. S3A and S3B) (21) shows that $HRAS^{G12V}$ and $KRAS^{G12D}$ are similar, where the valine and aspartic acid side chains point away from the nucleotide binding pocket. This is in contrast to $KRAS^{G12R}$, where the arginine side chain points directly into the pocket. Thus, $HRAS^{G12V}$ and $KRAS^{G12D}$ but not $KRAS^{G12R}$ retain an ordered SII region (Fig. 3G and H). Comparison of our GMPPNP-bound $KRAS^{G12R}$ structure with a previously determined GMPPNP-bound $HRAS^{G12R}$ structure (Supplementary Figs. S3C) (16) shows similar side chain conformations and interactions formed by R12, resulting in equivalent disruptions in SII and Q61/E62, and no significant isoform-specific structural differences were detected. Further, no differences in thermal stability between the G12 mutants and $KRAS^{WT}$ were observed, as measured by monitoring nucleotide binding as a function of temperature (Supplementary Fig. S3D).

$KRAS^{G12R}$ Is Impaired in PI3K-AKT Activation

As we observed a decrease in SOS^{cat} binding to $KRAS^{G12R}$, we hypothesized that $KRAS^{G12R}$ would exhibit altered effector specificity, potentially accounting for the inability of $KRAS^{G12R}$ to stimulate macropinocytosis. First, we utilized well-characterized RAS mutants (T35S, E37G and Y40C) that are differentially impaired in interaction with the major RAS effectors (22–24) to determine which pathways were critical for RAS-driven macropinocytosis. However, $KRAS^{G12D}$ and $KRAS^{G12V}$ carrying co-mutations at any of the three effector-binding domain residues failed to stimulate macropinocytosis in RIE-1 cells (Supplementary Figs. S4A–C), suggesting that multiple effector pathways are involved in driving KRAS-dependent macropinocytosis.

Second, we utilized reverse phase protein array (RPPA) analyses (25) to profile RIE-1 cells overexpressing KRAS G12 mutants, providing an isogenic background to evaluate KRAS signaling. Surprisingly, the only statistically significant effector signaling defect observed in the G12R-expressing cells was in the PI3K-AKT pathway (Fig. 4A; Supplementary Fig. S4D). Phosphorylation of AKT and AKT substrates (PRAS40, MDM2, FKHR and S6K) was decreased in cells expressing $KRAS^{G12R}$ relative to G12D or G12V (Fig. 4B and Supplementary Fig. S4E). We verified the RPPA results by immunoblot analysis and found that both basal and serum-stimulated activation of AKT were elevated (30–59%) in RIE-1 cells stably expressing $KRAS^{G12D}$ or $KRAS^{G12V}$ compared with control cells, whereas it was suppressed in $KRAS^{G12R}$-expressing cells (Fig. 4C and D). In contrast, MEK-ERK activation was elevated similarly in cells expressing each of the three mutants (Fig. 4E).

$KRAS^{G12R}$ is Unable to Bind to p110α

The decreased phosphorylation of AKT and its downstream substrates in $KRAS^{G12R}$-expressing RIE-1 cells suggested that $KRAS^{G12R}$ may be impaired in binding to and/or activating the catalytic subunit of PI3Kα (p110α), an upstream activator of AKT and validated driver of macropinocytosis (26). To directly address this possibility, we utilized a

well-characterized fluorescence-based solution-phase assay (27) to measure the dissociation constants of $KRAS^{WT}$, $KRAS^{G12D}$ and $KRAS^{G12R}$ with recombinant full-length p110α as well as the isolated RAS binding/association (RBD/RA) domains of RAF and other effectors. In agreement with previous studies (15), the dissociation constant of CRAF-RBD with $KRAS^{WT}$ was 61.0 ± 0.53 nM, which was decreased ~8-fold in $KRAS^{G12D}$ and $KRAS^{G12R}$. The dissociation constant of p110α with $KRAS^{WT}$ and $KRAS^{G12D}$ was ~2 μM, however, we did not detect any interaction between p110α and $KRAS^{G12R}$ (Fig. 4F and G). Dissociation constants of the isolated RA domains from RGL2 and PLCε were comparable among all KRAS mutants tested (Supplementary Fig. S4F).

To determine if the inability of $KRAS^{G12R}$ to stimulate macropinocytosis is due solely to its impaired interaction with p110α, we investigated whether co-expression of a membrane-targeted and constitutively activated p110α variant (p110α-CAAX) (28) would rescue macropinocytosis. While expression of p110α-CAAX alone was not sufficient to stimulate macropinocytosis (Figs. 4H–J), co-expression of p110α-CAAX with $KRAS^{G12R}$ in RIE-1 cells stimulated macropinocytosis to levels similar to those observed with $KRAS^{G12D/V}$ alone. As expected, co-expression of p110α-CAAX did not further enhance macropinocytosis in $KRAS^{G12D/V}$-expressing cells. Similarly, activation of endogenous PI3K signaling using insulin was only sufficient to elevate macropinocytosis in RIE-1 cells expressing $KRAS^{G12R}$ (Figs. 4H–J). Conversely, treatment with AZD8186, a PI3Kα/β inhibitor, decreased macropinocytosis in RIE-1 cells expressing $KRAS^{G12D/V}$ (Figs. 4K–M). Thus, we conclude that the inability of $KRAS^{G12R}$ to stimulate macropinocytosis in RIE-1 cells can be attributed solely to its impaired interaction with p110α.

$KRAS^{G12R}$ PDAC Exhibits Decreased PI3K-AKT Signaling

As $KRAS^{G12R}$ fails to bind p110α *in vitro*, we speculated that $KRAS^{G12R}$-mutant PDAC may also exhibit decreased PI3K signaling *in vivo*. Therefore, we applied RPPA to $KRAS^{G12R}$ PDAC cell lines to analyze the expression/activity of over 160 different signaling proteins (Fig 5A). While we observed that the RPPA profiles of $KRAS^{G12R}$-mutant cell lines clustered separately from $KRAS^{G12D/V}$-mutant cell lines, no clear mutation-specific signature was readily apparent (Supplementary Fig. S5A). Upon limiting our analysis to the 60 most differentially phosphorylated/expressed protein features (30 increased, 30 decreased), two prominent distinctions were observed in $KRAS^{G12R}$-mutant cell lines: upregulated levels of MYC and downregulation of signaling through PI3K-AKT-mTORC1-S6K-S6 (Fig. 5A).

Given that MYC is a critical KRAS effector in glucose metabolism (29), we sought to determine what role, if any, MYC plays in macropinocytosis and survival of $KRAS^{G12R}$-mutant PDAC cell lines. As we recently determined for $KRAS^{G12D/V}$-mutant PDAC (30), the growth of $KRAS^{G12R}$-mutant PDAC was also MYC-dependent (Supplementary Fig. S5B). However, transient knockdown of MYC reduced macropinocytosis in $KRAS^{G12D/V}$- but not $KRAS^{G12R}$-mutant cell lines (Fig. 5B and C; Supplementary Fig. S5C). Furthermore, as we recently described (30), MYC protein stability is dependent on KRAS activity. Consistent with this premise, transient knockdown of KRAS decreased MYC protein levels in all PDAC cell lines, independent of the specific KRAS mutation (Fig. 5D).

We then sought potential connections among the top 30 proteins that were the most decreased in phosphorylation or expression according to RPPA pathway mapping (Fig. 5A and S5A). Utilizing the Reactome pathway database and bioinformatics tools to identify signaling relationships among these proteins in an unbiased manner (https://reactome.org/) (31), we again found that the most decreased proteins were related to PI3K-AKT-mTOR signaling (Fig. 5E). Going back to the RPPA analyses, we found that the absolute RPPA intensities of these proteins were significantly decreased in the $KRAS^{G12R}$ PDAC cell lines compared to the $KRAS^{G12D}$ lines (Fig. 5F).

PI3K Signaling Is Required for Macropinocytosis in $KRAS^{G12R}$-mutant PDAC

Despite the inability of $KRAS^{G12R}$ alone to drive macropinocytosis in a variety of cell models, *KRAS*^{G12R}-mutant PDAC cell lines nevertheless exhibited robust macropinocytosis (Fig. 1A). As we had determined that the inability of $KRAS^{G12R}$ to drive macropinocytosis in cell models was due solely to loss of p110α activation, we then addressed the possibility that another PI3K isoform activated independently of KRAS may compensate for this deficiency. Whereas expression of the p110α-related PI3K catalytic subunit isoforms p110δ and p110γ is generally restricted to hematopoietic cells (32), both isoforms are upregulated in PDAC (Fig. 6A) (33). To address their potential role in macropinocytosis, we utilized PI3K isoform-selective inhibitors. As expected, the pan-PI3K kinase inhibitor pictilisib (p110α/β/δ/γ) significantly reduced macropinocytosis in all KRAS-mutant PDAC cell lines tested (Fig. 6B), supporting the requirement for PI3K activity in this process. The p110α-selective inhibitor alpelisib and the p110α/β inhibitor AZD8186 reduced macropinocytosis only in *KRAS*$^{G12D/V}$-mutant lines but had no effect in any of the seven *KRAS*^{G12R}-mutant PDAC lines (Fig. 6B; Supplementary Fig. S6A and S6B, respectively), consistent with the inability of *KRAS*^{G12R} to activate p110α. Finally, the p110γ-specific inhibitor IPI-549 not only decreased macropinocytosis in all $KRAS^{G12R}$-mutant lines, but unexpectedly, also did so in the $KRAS^{G12D/V}$-mutant lines (Fig. 6B). As expected, treatment with the pan-PI3K inhibitor reduced pAKT levels in all cell lines (Fig. 6C). However, treatment with the selective p110α or p110γ inhibitors did not result in a consistent reduction in pAKT levels that correlated with a reduction in macropinocytosis. These results indicate that PI3K but not AKT activity is required to support macropinocytosis.

Verifying the p110γ-specific activity of IPI-549, siRNA suppression of *PIK3CG* (encoding p110γ) reduced macropinocytosis in all cell lines evaluated, regardless of the specific KRAS mutation (Fig. 6D). Coupled with our evidence that macropinocytosis in $KRAS^{G12R}$-mutant PDAC lines is KRAS independent (Fig. 1B–D), this result indicates that p110γ contributes to macropinocytosis regardless of whether that process is KRAS-dependent or -independent. Further, PI3K can activate the RAC1 small GTPase, a known regulator of RAS-dependent macropinocytosis, through activation of RACGEFs (e.g., PREX1/2) (34). In agreement with previously published results (35,36), transient siRNA suppression of *RAC1* reduced macropinocytosis in all lines tested, irrespective of KRAS mutation status (Fig. 6E).

$KRAS^{G12R}$ Mutation Alone Is Not Predictive of Sensitivity to MAPK Inhibition

Given that $KRAS^{G12R}$ displayed impaired p110α binding and PI3K signaling, and that the PI3K-AKT axis is a known driver of resistance to inhibitors of the ERK MAPK cascade

(37), we speculated that $KRAS^{G12R}$-mutant PDAC cells may be preferentially sensitive to inhibitors of the MEK-ERK pathway compared to PDAC cells expressing KRAS mutants that retain the ability to activate p110α. To address this possibility, we analyzed a panel of 52 PDAC cell lines treated with the MEK1/2-selective inhibitor selumetinib. Mean activity area (AA) was obtained from four-parameter drug response curves (Fig. 6F) and integrates IC_{50} (Fig. 6G) with maximum response (A_{max}) at the highest drug concentration (AA = Σi[0-min(0,Ai/100)). There was >80% agreement between AA and IC_{50} values in classifying cell lines as sensitive (AA≥2.5; IC_{50}<1 μM) or resistant (AA<1.8; IC_{50}≥10 μM) (Supplementary Fig. S6C and S6D). On average, PDAC cell lines harboring $KRAS^{G12R}$ mutations were more sensitive to MEK inhibition than those harboring other KRAS mutations, yielding higher AA values and lower IC_{50} values.

To exclude the possibility that other genetic mutations associated with KRAS mutational status might drive the selumetinib drug-response phenotype, we determined the mutation status of the 250 most common cancer genes in all 52 cell lines. Like the large genotyping efforts of TCGA and ICGC on clinical specimens, we found that *TP53* (34/52), *CDKN2A* (8/52) and *SMAD4* (8/52) genes followed *KRAS* as the most commonly mutated genes in PDAC (Supplementary Fig. S6E). We did not find a significant co-occurrence of mutations specific to the $KRAS^{G12R}$ cell lines among the 250 genes analyzed, including single nucleotide variants or small insertions and deletions.

Utilizing additional model systems, we found that growth of $KRAS^{G12R}$-mutant PDAC organoids were more sensitive than $KRAS^{G12D}$-mutant organoids to MEK1/2 inhibition (selumetinib; EC_{50} of 12.3 nM vs. 575 nM, Fig. 6H and I). Lastly, we transplanted PDAC patient-derived xenograft (PDX) tumors into immunocompromised mice and treated them with 35 mg/kg selumetinib twice daily for 28 days. Prior to treatment (F3 or F4 generation; F0, surgical resection specimens; tumor volume 200–250 mm^3), these PDX tumors retained most cytoarchitectural features of the original patient tumor, including a significant human stromal component (Fig. 6J and K). Selumetinib suppressed growth of the $KRAS^{G12R}$-mutant PDX tumors to a significantly greater extent than the $KRAS^{G12D}$-mutant tumors (Fig. 6L and M). To confirm that growth suppression was related to the mechanism of action of selumetinib, we examined phospho-ERK, cyclin D1 (T286) and $p27^{KIP1}$ (T187) in untreated and treated tumors. Inhibition of MEK induces G_1/S cell cycle arrest via a reduction of cyclin D1 and the induction and stabilization of $p27^{KIP1}$. While phosphorylated cyclin D1 levels (T286) were slightly elevated in both tumor sets, quantitative RPPA profiling of pooled lysates from tumors (n=6 per group) showed effective inhibition of ERK phosphorylation in both PDX models with no difference in the induction of $p27^{KIP1}$ levels between the two models (Fig. 6N and O). In summary, selumetinib achieved MEK inhibition in the xenotransplanted mice.

Finally, since we previously found that KRAS-mutant PDAC cell lines displayed inconsistent sensitivities to MEK versus ERK inhibition (11), we also utilized the ERK1/2-selective inhibitor SCH772984 (ERKi) in five $KRAS^{G12D}$ and five $KRAS^{G12R}$-mutant PDAC organoids. ERK inhibition was moderately more effective at inhibiting the proliferation of $KRAS^{G12R}$ vs. $KRAS^{G12D}$ PDAC; however, the difference was not statistically significant (Supplementary Fig. S7A–C). In summary, a subset of $KRAS^{G12R}$-

mutant PDAC models exhibited increased sensitivity to MEK or ERK inhibition compared to KRAS^{G12D}-mutant PDAC. Overall, the effect was modest and we could not conclude that *KRAS*^{G12R} mutation status alone provides a definitive genetic marker to merit single-agent treatment of PDAC patients with MEK or ERK inhibitors.

KRAS^{G12R}-Mutant PDAC Exhibit a Distinct Drug Sensitivity Profile

To assess whether KRAS^{G12R}- and KRAS^{G12D}-mutant PDAC exhibit differential sensitivity to other oncology drugs, we performed a 525-inhibitor drug sensitivity and resistance testing (DSRT) analysis on seven KRAS^{G12R} PDAC lines and compared the results to 16 KRAS$^{G12D/V}$-mutant PDAC cell lines (Supplementary Fig. S8A). In this assay, the KRAS^{G12R}-mutant lines showed a trend towards increased sensitivity to MEK/ERK inhibition compared to the KRAS$^{G12D/V}$-mutant lines, and surprisingly, they were significantly more sensitive to PI3K inhibition, likely due to the lack of KRAS signaling through this pathway (Fig. 7A). Given the DSRT results and unique dependence on PI3Kγ in KRAS^{G12R} cell lines, we asked whether KRAS^{G12R}-mutant organoids would be more susceptible to concurrent ERK MAPK and PI3Kγ inhibition. In agreement with the DSRT and macropinocytosis data, KRAS^{G12R}-mutant organoids showed increased sensitivity to PI3Kγ inhibition (hT2 EC_{50} = 2.6 μM vs. hM1A, resistant) and combined ERK MAPK and PI3Kγ inhibition was synergistic in the KRAS^{G12R}-mutant organoid line (Supplementary Fig. 8B and C).

We recently determined that concurrent inhibition of ERK1/2 and autophagy synergistically suppressed the growth of KRAS-mutant PDAC (38), leading to our initiation of clinical trials to evaluate the combination of MEK or ERK inhibitor together with the autophagy inhibitor hydroxychloroquine. In the present study, we noted from our DSRT analyses that KRAS^{G12R} PDAC showed increased single-agent sensitivity to both chloroquine and mepacrine compared to KRAS$^{G12D/V}$ lines (Fig. 7A). We speculated that this may be due to the impaired ability of KRAS^{G12R} to activate PI3K-AKT-mTORC1 signaling, which suppresses autophagy (9). We further speculated that KRAS^{G12R} PDAC lines may be hypersensitive to this combination. To directly determine if KRAS^{G12R} and KRAS^{G12D} differ in their regulation of autophagy, we applied the dual fluorescence autophagic flux assay to RIE-1 cells stably expressing the different KRAS mutants. As we observed previously (38), autophagy was suppressed in KRAS$^{G12D/V}$-expressing cells relative to empty vector control cells. In contrast, autophagy was not suppressed in KRAS^{G12R}-expressing cells (Supplementary Figs. S8D–F). Thus, KRAS^{G12R} is impaired in regulation of two distinct lysosome-associated metabolic activities: macropinocytosis and autophagy.

We next determined whether KRAS^{G12R}-mutant PDAC lines are more sensitive to combined ERK and autophagy inhibition. As expected, chloroquine alone was sufficient to decrease cell viability, but had no effect on cytotoxicity as a single agent (Fig. 7B). However, the decrease in viability upon dual treatment with ERK inhibitor plus chloroquine was only additive, with markedly less synergy than observed in non-KRAS^{G12R}-mutant PDAC cell lines (Fig. 7B), yet the combination increased cytotoxicity in most of the KRAS^{G12R} cell lines. Finally, in addition to chloroquine, a non-specific inhibitor of autophagy, we also tested two ULK-specific inhibitors, which block the initiating kinases of the autophagic

cascade and have been shown to reduce autophagy in PDAC (38). Both ULK inhibitors, MRT68921(ULK1/2i; Fig. 7C) and SBI0206965 (ULK1i; Fig. 7D), were more effective than chloroquine at reducing cell viability when combined with ERKi, and ULK1/2i was synergistic with ERK inhibition in four out of five $KRAS^{G12R}$ mutant PDAC cell lines. Thus, we speculate that, although $KRAS^{G12R}$ activation of p110α is impaired, the compensatory activation of p110γ that allows $KRAS^{G12R}$ to potently drive PDAC growth also minimizes its differential drug sensitivity, as revealed in the DSRT analysis (Supplementary Fig. 8A), compared with $KRAS^{G12D}$ PDAC.

DISCUSSION

The $KRAS^{G12R}$ mutation is rare in cancer overall, yet found at high prevalence in PDAC. Further, $KRAS^{G12R}$ mutations in PDAC are associated with additional co-occurring KRAS mutations (6) and $KRAS^{G12R}$ status is correlated with better overall survival (13 months) compared to $KRAS^{G12D}$ (8 months) or $KRAS^{G12V}$ (10 months) (39), supporting our premise that the $KRAS^{G12R}$ mutation may have driver functions that are distinct from the more common G12 mutants. We therefore evaluated the cellular and biochemical properties of $KRAS^{G12R}$. Surprisingly, $KRAS^{G12R}$ fails to interact with and activate a key effector, p110α PI3K, essential for KRAS-driven cancer development (40). Additionally, $KRAS^{G12R}$ is impaired in stimulating macropinocytosis, a metabolic activity critical for PDAC tumor growth (10). However, we found that overexpression of the related p110γ PI3K compensates for the impaired promotion of macropinocytosis by $KRAS^{G12R}$, providing a possible explanation for the unusually common occurrence of this KRAS mutation in PDAC.

While there are six possible single-base change mutations at codon 12, their overall frequencies are widely divergent. Until recently, it was assumed that the basis for this was due to different susceptibilities to mutational insults. The $KRAS^{G12C}$ mutation, which is found at a high frequency in smoking-associated lung cancers but not in other cancers (1), provides strong evidence for this premise. However, complicating this issue are tissue-specific differences, for example that $KRAS^{G12R}$ is rare in cancer overall yet common in pancreatic cancer. Thus, an alternative hypothesis states that the biological potency of each KRAS mutant protein drives cancer development and thereby dictates how common or rare a given mutation will be. Our finding that $KRAS^{G12R}$, unlike the more prevalent G12D or G12V mutant proteins, failed to bind and activate a key effector, PI3Kα, supports a biological basis for the low prevalence of this mutation overall in cancer. As we discuss below, we also identified a possible basis for how $KRAS^{G12R}$, despite this defect, can still effectively drive PDAC development and growth. In summary, our findings, together with other recent studies (41,42), support the importance of oncogenic potency in driving the differential frequency of specific RAS mutations seen in cancers that arise from different tissues.

The RAS-PI3Kα interaction has been shown to be necessary for tumor growth: ablation of RAS interaction with p110α reduced tumor initiation and maintenance in RAS-driven lung and skin cancer (7,43). Therefore, while impaired engagement with PI3Kα may provide a biological basis for the rarity of $KRAS^{G12R}$ mutations in other KRAS mutant-associated cancers, such as lung and colorectal cancer, conversely, why $KRAS^{G12R}$ constitutes the third

most prevalent KRAS mutation in PDAC has been puzzling. Our studies identified two possible KRAS-independent activities that enable $KRAS^{G12R}$ mutations to be more common in PDAC compared to other cancer types.

We showed that ectopic expression of activated PI3Kα rescued the macropinocytosis defect seen when $KRAS^{G12R}$ was evaluated in cell models, arguing that this mutant was defective solely in activation of PI3Kα. In PDAC, a possible mechanism to restore PI3K signaling may be exogenous insulin from pancreatic endocrine tissue acting on adjacent tumor cells. However, this would not explain the growth of metastatic $KRAS^{G12R}$-mutant PDAC in non-pancreas tissue. Thus, other mechanisms that activate PI3K may also restore the potent cancer-driving functions of $KRAS^{G12R}$.

Another mechanism we identified in $KRAS^{G12R}$-mutant PDAC involved over-expression of the related isoform p110γ. Consistent with this compensatory mechanism, whereby p110γ provides the functions of both p110γ and p110α, we found that treatment with a p110γ- but not p110α-selective inhibitor blocked macropinocytosis. However, in $KRAS^{G12D}$-mutant PDAC cells, a p110α- or p110γ-selective inhibitor (or a pan-PI3K inhibitor) were all capable of blocking macropinocytosis, indicating that both α and γ isoforms were active and required in this context. Studies in *Dictyostelium discoideum* have shown that distinct isoforms of PI3K serve distinct roles in supporting macropinocytosis, with one isoform driving cup formation and the other cup closure (26). Similarly, macropinocytosis in $KRAS^{G12D}$-mutant PDAC cells may require distinct functions of different PI3K isoforms.

We observed that MYC protein stability is regulated by both $KRAS^{G12D}$ and $KRAS^{G12R}$, and that both $KRAS^{G12D}$- and $KRAS^{G12R}$-mutant PDAC cell lines retain MYC-dependent growth. However, macropinocytosis was dependent on MYC in $KRAS^{G12D}$- but not $KRAS^{G12R}$-mutant PDAC cell lines. This connection between MYC and macropinocytosis in $KRAS^{G12D}$-mutant PDAC was unexpected, as no association between them has been described previously.

Another surprising finding from our studies was that the lack of elevated macropinocytosis when $KRAS^{G12R}$ was ectopically expressed in simple cell models was not reflected in bona fide cancer cells endogenously harboring $KRAS^{G12R}$ mutations. Indeed, macropinocytosis was elevated in both $KRAS^{G12R}$- and $KRAS^{G12D}$-mutant PDAC cell lines, consistent with the critical role of macropinocytosis in pancreatic cancer growth (10). However, in the $KRAS^{G12R}$-mutant cell lines, this elevation was KRAS-independent. An important lesson learned is that the model systems are useful in demonstrating what a given KRAS mutant can or cannot do alone, but the phenotypes observed do not necessarily reflect what will occur in tumor cells expressing that same mutant in a context that is genetically and epigenetically more complex.

Upon identifying defective PI3Kα signaling by $KRAS^{G12R}$, an activity associated with driving resistance to ERK MAPK inhibition, we anticipated that we might be able to identify a therapeutic approach that would be preferentially effective in $KRAS^{G12R}$-mutant PDAC. Taking both candidate and unbiased approaches, we found that $KRAS^{G12R}$-mutant PDAC showed increased sensitivity to inhibition of ERK MAPK or autophagy compared to

$KRAS^{G12D}$-mutant PDAC. We speculated that perhaps $KRAS^{G12R}$-mutant PDAC may be hypersensitive to combined inhibition of ERK MAPK and autophagy, which we recently identified as an effective therapeutic strategy for $KRAS^{G12D/V}$ mutant PDAC (38). We were surprised that, whereas this combination synergistically suppressed the growth of $KRAS^{G12D}$-mutant PDAC, it was only additive in $KRAS^{G12R}$-mutant PDAC. Although all KRAS-mutant PDAC are responsive to this combination, and as trials have begun and are planned with combinations that inhibit MEK or ERK and autophagy, other genetic markers will be needed beyond specific KRAS mutational status, to stratify patients for treatment with these combinations.

METHODS

Cell Lines

PATC43 and PATC50 cell lines were provided by J. Fleming (MD Anderson Cancer Center); RWP1, FA6 and Paca44 were from N. Lemoine (Barts Cancer Institute, London, UK); IMIM-PC-1, SK-PC-1 and SK-PC-3 from F. Real (Center Nacional de Investigaciones Oncologicas, Spain); MDAPanc-48 and MDAPanc-81 from E. Frazier (MD Anderson Cancer Center); L3.3 and FG from I. Fidler (MD Anderson Cancer Center); A818 from H. Kalthoff (University of Kiel, Germany); PSN.1 from the European Collection of Authenticated Cell Cultures (ECACC); SNU-213, −324 and −410 from the Korean Cell Line Bank; HuP-T3, HuP-T4, YAPC, DAN-G and PaTu-8988T from the DSMZ German Collection of Microorganisms and Cell Cultures; PACADD-135, −159, −165 and −183 from F. Rueckert, (University Hospital Carl Gustav Carus, Technische Universität Dresden, Germany); KP-2, −3 and TCC-Pan2 from the Japanese Collection of Research Bioresources Cell Bank; PK-1, PK-8, PK-45P, PK-59, KP-4, NOR-P1 and T3M-4 from Riken Cell Bank; SB.rb and SB.bm were primary patient-derived pancreas cancer cell lines from our institution (U. Rudloff, NCI). The remaining PDAC cell lines were obtained from ATCC and were maintained in either Dulbecco's Modified Eagle Medium (DMEM) or RPMI 1640 supplemented with 10% fetal bovine serum (FBS). The model cell lines (HPNE-DT, HEK293T and RIE-1) were all maintained in DMEM supplemented with 10% FBS. All cell lines were maintained in a humidified chamber with 5% CO_2 at 37°C. Cell lines used in experiments were passaged for one month or 10 passages before a new aliquot was thawed. Cell line authenticity was verified by short tandem-repeat (STR) profiling (04.17.2017) and all lines were monitored monthly for mycoplasma contamination using the Lonza MycoAlert™ Mycoplasma Detection Kit.

Macropinocytosis

Macropinocytosis was performed as previously described (10). Cells were incubated for 30 min with 50 μg/ml or 100 μg/ml DQ-BSA, followed by a 90-min chase in serum-free DMEM/RPMI before fixation. Approximately 50–100 cells in nine-to-twelve fields-of-view per condition were imaged on a Zeiss 700 confocal microscope (63x, 1.4 N.A. objective). For overall macropinocytosis levels in PDAC cells, power and gain levels were determined using the AsPC-1 cell line. For RIE-1 cells, power and gain levels were set using the $KRAS^{G12D}$ condition in each experiment. For conditions where siRNA, inhibitors or other treatments were applied, power and gain levels for each cell line were set using the

corresponding control condition. The cell outline was mapped using a differential interference contrast image. Macropinocytotic index was quantified using ImageJ by taking the macropinosome area divided by the total cell area and multiplying by 1000.

Retroviral and Lentiviral Vector Infections

Human KRAS4B mutant proteins and membrane-targeted, constitutively activated chimeric p110α terminating in the HRAS C-terminal "CAAX" membrane targeting sequence (28) were ectopically expressed from the retroviral expression vector pBabe in RIE-1, NIH/3T3 and HPNE-DT cells. The doxycycline-inducible lentiviral expression vector pInducer was used to ectopically express siRNA-resistant KRAS4B mutants in AsPC-1 and Pa04C PDAC cells. Viral particles were generated by transient transfection of each expression vector into HEK293T cells using Fugene6 (Promega) with the pCL-10A1 packaging system for retrovirus or the psPAX2 and pMD2.G packaging system for lentivirus, according to the manufacturer's recommended protocol. Infection of cell lines was performed in growth medium supplemented with 8 mg/ml polybrene.

siRNA Treatment of Cell Lines

siRNA Silencer® Select oligonucleotides against scrambled (Negative Control No. 1), KRAS (s7940, s7939), MYC (s9129, s9130), p110γ (s10533, s10534) and RAC1 (s11711, s11712) sequences were obtained from Invitrogen and transfected into cells by using Lipofectamine RNAiMAX following the manufacturer's recommended protocol. After 16 h, the medium was exchanged, representing time 0 for siRNA-mediated knockdown.

2D and 3D Growth Assays of PDAC cell lines

To study the effect of *KRAS* silencing on growth, cells were treated for 48 h with a KRAS-specific siRNA, trypsin-digested, counted and plated. To measure growth on plastic, cells were plated in duplicate in 6-well dishes at a density of 2×10^3 (MIA PaCa-2 and AsPC-1), 3×10^3 (A818–4, PSN-1 and PK-8) or 5×10^3 (Pa04C, PATC43, PATC50, TCC-PAN2 and HuP-T3) cells per well. Plates were developed after seven days by removing the medium and fixing cells with 4% paraformaldehyde and crystal violet. To monitor 3D proliferation, 50 μl 0.6% bacto agar per well was placed into clear-bottom 96-well plates. Cells were mixed into 1% SeaPrep agarose and plated at a density of 5×10^3 (MIA PaCa-2 and AsPC-1), 7.5×10^3 (A818–4 and PK-8) or 1×10^4 (Pa04C, PATC43, PATC50, PSN-1, TCC-PAN2 and HuP-T3) cells per well. To quantitate cell number, cell viability was determined by staining with AlamarBlue® after seven days, according to the manufacturer's protocol. Each biological replicate experiment included four technical repeats for each cell line. A corresponding 6-well plate was generated for western blot analysis to verify KRAS knockdown.

Organoid Culture Conditions

Organoids (hM1A and hT2) were kindly provided by the Tuveson laboratory (Cold Spring Harbor Laboratory). Organoids were cultured at 37°C in 5% CO_2. Cells were seeded in growth factor-reduced Matrigel (Corning; Cat# 356231) domes and fed with human complete feeding medium: advanced DMEM/F12-based WRN-conditioned medium (L-

WRN (ATCC CRL-3276)), 1x B27 supplement, 10 mM HEPES, 0.01 μM GlutaMAX, 10 mM nicotinamide, 1.25 mM N-acetylcysteine, 50 ng/mL hEGF, 100 ng/mL hFGF10, 0.01 μM hGastrin I, 500 nM A83–01, 1 μM PGE2 and 10.5 μM Y27632 (44).

Organoid Inhibitor Treatment and Viability Assay

Organoids were generated under Institutional Review Board (IRB)-approved protocols at Dana-Farber Cancer Institute (DFCI #14–408, 17–000) or Cold Spring Harbor Laboratory using previously published protocols (44,45). All patients provided written informed consent, and the studies were conducted in accordance with recognized ethical guidelines. Organoids were cultured at 37°C in 5% CO_2. Organoids were dissociated and 3000–5000 single cells per well were seeded in 150 μl of 10% growth factor-reduced Matrigel (Corning) and 90% human organoid feeding medium + 10.5 μM Y27632 (Selleckchem) into poly(2-hydroxyethyl methacrylate)-coated clear flat-bottom 96-well plates (Corning Ref. 3903). Two days after seeding, organoids were treated with ERKi SCH772984 (0 nM to 10 μM) or MEKi AZD6244 (selumetinib) (0 to 2.5 μM), randomized on a Tecan D300e drug dispenser. On day seven, the perimeter wells were refilled with 1X PBS. Ten days after inhibitor treatment, organoids were imaged with a Molecular Devices SpectraMax i3x MiniMax 300 imaging cytometer. After image acquisition, organoid viability was assessed using the Cell-TiterGlo 3D Cell Viability Assay (Promega; Cat# G9683) on a SpectraMax i3x (UNC) or Clariostar Plate Reader (LC-3200; DFCI) plate reader according to the manufacturer's protocol. Depending on the assay, duplicate or triplicate measurements were recorded for each inhibitor concentration.

Immunoblotting

Cells were washed twice with ice-cold PBS, lysed in 1% NP-40 buffer (25 mM Tris-HCl, pH 7.4, 100 mM NaCl, 10 mM $MgCl_2$, 1% NP-40) supplemented with phosphatase (Sigma) and protease (Roche) inhibitors, scraped and collected in chilled Eppendorf tubes. Lysates were cleared by centrifugation at 15,000 × g for 15 min at 4 °C, and the protein concentration was determined using Bradford assay (Bio-Rad). Standard immunoblotting procedures were followed. Membranes were blocked in 5% milk diluted in TBS with 0.05% Tween 20 (TBST). To determine the levels of activated proteins, blot analyses utilized phospho-specific antibodies to AKT (T308 and S473), p70S6K (T389), MEK1/2 (S217/S221), ERK1/2 (T202/Y204) and RSK (T359/S363) (Cell Signaling Technologies, CST), with corresponding antibodies recognizing total proteins, as well as p110 (all isoforms), RAC1 and MYC (CST) to measure total protein levels. Immunoblotting for total KRAS (Sigma) protein was done to verify siRNA suppression and for GAPDH (CST) and vinculin (Sigma) to verify equivalent loading of total cellular proteins. Anti-HA antibody (Covance) was used to probe for overexpressed KRAS.

Flow Cytometry

Apoptosis analyses were performed using the TACS® Annexin V-FITC Kit (Trevigen, Inc.) following the manufacturer's protocol. Briefly, spent culture medium containing detached cells was collected, mixed with trypsinized cells and centrifuged at 300 × g for 5 min. After washing once in ice-cold 1X PBS, cells were incubated in Annexin V Incubation Reagent (1% Annexin V-FITC, 1X propidium iodide solution, in 1X calcium-containing binding

buffer) at RT for 15 min in the dark before diluting with 1X binding buffer. Cells were analyzed on a BD LSRFortessa flow cytometer, and data were collected and exported using FACSDiva v8.0.1 and analyzed with Cytobank. Using an SSC-A (y) vs FSC-A (x) dot plot, a "cells" gate was used to exclude small and large debris. Cells were analyzed for apoptosis in a PI-A (y) vs FITC-A (x) dot plot and a quadrant gate was established around the healthy population of DMSO control cells (PI-A negative, FITC-A negative). For cell cycle analysis, cells were harvested, washed once in PBS and suspended in fresh PBS. Ten volumes of ice-cold 70% ethanol were added to each tube dropwise while gently vortexing. Cells were incubated overnight at 4°C. The fixed cells were washed once in PBS and suspended in PBS containing 40 μg/ml propidium iodide (Life Technologies, Inc.) and 100 μg/ml RNase A (Life Technologies, Inc.). Cells were incubated for 2–3 h at 37°C and analyzed using FACSDiva v8.0.1 on a BD LSRFortessa flow cytometer. After separating cells from debris in an SSC-A (y) vs FSC-A (x) dot plot, doublets were excluded with a FSC-H (y) vs FSC-A (x) dot plot. Singlet cells were analyzed for propidium iodide staining to determine DNA content at 2N (G0/G1), 4N (G2/M), or in between (S). Data were analyzed with the Multicycle DNA algorithm in FCSExpress.

Sample Preparation and Reverse Phase Protein Microarray (RPPA)

Samples for RPPA analyses were prepared and performed as previously described (46). In brief, cell lysates were prepared and arrayed on an Aushon 2470 automated system (Aushon BioSystems). Selected arrays were stained with Sypro Ruby Protein Blot Stain (Molecular Probes) following manufacturer's instructions to quantify the total protein. Remaining arrays were pre-treated with Reblot Antibody Stripping solution (Chemicon) for 15 min at RT, followed by two washes with PBS and incubated for 5 h in I-block (Tropix) prior to antibody staining (47). Using an automated system (DakoCytomation), arrays were incubated with 3% hydrogen peroxide, biotin blocking system and an additional serum-free protein block to reduce nonspecific binding. Each array was probed for 30 min with one antibody targeting the protein of interest. Arrays were probed with a total of 157 antibodies previously tested for their specificity and ability to capture the linear dynamic range of the protein of interest (48,49). Biotinylated anti-rabbit (Vector Laboratories, Inc.) or anti-mouse secondary antibody (DakoCytomation) coupled with a commercially available tyramide-based avidin/biotin amplification system (Catalyzed Signal Amplification System (CSA), DakoCytomation) were used for signal amplification. Fluorescent detection was achieved using the IRDye 680RD Streptavidin (LI-COR Biosciences) system. Sypro Ruby and antibody stained slides were scanned on a Tecan laser scanner (TECAN) using the 580 nm and 620 nm channels. Images were analyzed using commercially available software (MicroVigene Version 5.1.0.0, Vigenetech) as previously described (50).

Supervised hierarchical clustering was performed using R (version 3.4.1). The heatmap, containing the 60 most differentially expressed protein features, was generated using the ComplexHeatmap package. The RPPA standardized intensity data were $\log_2$ transformed, and the median of three independent biological replicates was determined for each feature. Data from cells harboring $KRAS^{G12D}$ or $KRAS^{G12R}$ mutations were separated into two groups. A Wilcoxon rank sum test was applied to identify the top 30 and bottom 30 features that were most differentially expressed between the two groups, out of the 162 total protein

features evaluated. Heatmaps were row-normalized using a Z-score. Rows and columns were clustered via hierarchical clustering (Euclidean distance).

Drug Response Testing

Cells (1,000–2,500 cells per well, depending on cell line) were seeded in 96-well plates and incubated for 24 h before addition of drug. Increasing concentrations of drug, with DMSO (vehicle) as a negative control, were added to the wells in three replicates using a digital dispenser liquid handling device (TECAN D300e). For the 525-inhibitor DSRT screen, plates were incubated at 37°C for 5 d after addition of drug and analyzed using the Promega CellTiter-Glo assay reagent (Promega). Plates were read on a GloMax® 96 Microplate Luminometer (Promega). Percent cell viability was calculated by normalizing raw luminescence values to vehicle-control (DMSO-treated) samples. For co-treatment with the ERK inhibitor and chloroquine or the ULK inhibitors, cells were stained with Calcein AM (Invitrogen) according to the manufacturers recommended protocol, and the wells were counted using a SpectraMax MiniMax 300 imaging cytometer. For survival curves, the average of 10 wells from a day 0 control plate was used to determine baseline viability while the average of the vehicle-control wells at day 5 was used to determine maximum viability. All data were analyzed using SoftMax version 5 and GraphPad Prism version 7.03 using a 4-parameter drug response curve. Generation of the dose-response curves as well as scoring and clustering the data were performed as previously described (51), using the cell lines indicated in the figure.

Patient-Derived Xenotransplantation Models

Patients provided written informed consent on IRB-approved protocol NCI 09-C-0179, and the studies were conducted in accordance with recognized ethical guidelines. All animal studies were conducted at the National Cancer Institute (NCI) in Bethesda, MD, according to protocols and policies of the Institutional Animal Care and Use Committees (IACUC). Immediately after surgical resection, 2×2 mm^2 fragments from viable tumor areas were implanted subcutaneously into the right flanks of 6 to 8-week old NOD-SCID mice (F0 generation). Tumor fragments were re-transplanted 2–3 times when tumors reached 2×2 cm^2 (F3 and F4 generation). When tumor volumes reached 200 mm^3, at least 10 mice per arm were treated by oral gavage with vehicle or selumetinib (35 mg) twice daily for 28 days. Tumor volume was measured twice weekly via bidirectional caliper measurements. Tumor lysates were obtained from harvested tumors after 28 days and subjected to RPPA analysis. In addition to H&E, tumors were stained for collagen type I (ab34710, Abcam), trichrome, smooth muscle actin (SMA) (#A2547, Sigma-Aldrich) and CD31 (ab28364) (Abcam). Brightfield images (immunostaining) were acquired using an Aperio ScanScope XT (Aperio) for whole slide scanning at 20X magnification and analyzed using ImageScope Microvessel Analysis.

Protein Purification

The cDNA sequence encoding truncated human KRAS4B (residues 1–169) was cloned into the pQlinkH bacterial expression vector (gift from Konrad Buessow; Addgene plasmid # 13667) containing an N-terminal 6x-His purification tag followed by a Tobacco Etch Virus (TEV) protease cleavage site (52). RASGRP1 (residues 50–468, pET28a) and SOS^{cat}

(residues 564–1049, pPROexHTb) contained a similar vector architecture. Bacterial expression vectors encoding KRAS-GTP effector interacting domains included CRAF-RBD (residues 54–131, pQlinkH), RGL2-RA (residues 647–736, pGEX3T-2) (53) and PLCε-RA (residues 2113–2221, pTriEx4) (54). All 6x His-tagged proteins were expressed in BL21 (DE3) Rosetta2 cells and purified following the Qiagen Nickel NTA purification protocol and the 6X-His tags were removed using TEV protease. For pGEX vectors, proteins were purified following the Glutathione Sepharose™ 4B purification protocol (Amersham Pharmacia Biotech). The GST-tag was cleaved overnight using thrombin protease while dialyzing in wash buffer. If necessary, the proteins were further purified by size exclusion chromatography (Superdex-75 10/300 GL column; GE Life Sciences) and judged greater than 95% pure by SDS-PAGE analysis. Insect cell-expressed full length human PI3K (p110α/p85) protein was provided by H. Li and J. Wu (Genentech) and expressed and purified as described previously (55).

Guanine Nucleotide Exchange and Protein Binding Assays

We performed nucleotide exchange by replacing GDP with nucleotide analogs. For loading GMPPNP and 2'-/3'-O-(N'-methylanthraniloyl)β,γ-methyleneguanosine 5′-triphosphate (mGMPPCP; Jena Biosciences), $KRAS^{G12R}$ was incubated with alkaline phosphatase beads and GMPPNP (20-fold excess) for 3 h with gentle rotation, followed by removal of alkaline phosphatase and purification using a desalting column. Purified protein was checked for nucleotide exchange by HPLC, which showed close to 95% replacement of the bound nucleotide (56). Exchange for 2'-/3'-O-(N'-methylanthraniloyl)GDP (mGDP;Jena Biosciences) was performed following previously published methods (57).

Nucleotide exchange assays were performed using a Cary Eclipse Fluorescence Spectrophotometer (Agilent), as previously described (57). The minimal catalytic fragment of the RASGEF SOS^{cat} or $GRP1^{cat}$ was used to stimulate nucleotide dissociation. All experiments were performed in triplicate.

The fluorescent GTP-binding assay was adapted from a previous protocol (58). In brief, KRAS loaded with mGppCp (1.5 μM) was incubated with increasing concentrations of CRAF-RBD, PLCε-RA or RGL2-RA in Buffer D (20 mM HEPES, 50 mM NaCl and 5 mM $MgCl_2$ at pH 7.4) or PI3Kα in assay Buffer D + 5% glycerol. Nucleotide dissociation was initiated by addition of 1000-fold excess of unlabeled nucleotide at 25°C. The rate-of-dissociation was monitored by the change in fluorescence at an excitation wavelength of 355 nm and emission at 448 nm, using a Spectramax M5 plate reader with a 384-well Greiner plate. Fluorescent nucleotide dissociation curves were fit to a one-phase exponential decay equation using GraphPad Prism version 7.03. The dissociation rate was fit against the ligand concentration using previously published methods (58). All experiments were performed in triplicate.

Thermal Melts

KRAS proteins were preloaded with mGDP as described. Using a Cary Eclipse Fluorescence Spectrophotometer with an attached circulating water bath (PCB-1500, Agilent), the temperature was ramped at 1°C/min from 25°C to 80°C while monitoring

mGDP fluorescence every 30 sec (excitation 365 nm, emission 435 nm). A cuvette containing only mGDP was used as a control, where the intrinsic fluorescence loss over temperature was fit to a linear curve and added to the KRAS curves to correct for fluorescence quenching due to temperature change. The resulting curve was transformed by a first derivative, and the T_m was calculated from the inflection point.

Crystallization and Structure Determination

Concentrated $KRAS^{G12R}$ bound to GMPPNP was used for crystallization screening. The final crystallization buffer consisted of 2.1 M sodium malonate pH 7.5 and 40 mM dimethyl octylphosphine oxide. For data collection, crystals were flash frozen (100 K) in the mother liquor supplemented with 30% (v/v) sodium malonate pH 7.0 as a cryoprotectant. The diffraction data were collected using synchrotron radiation at beamlines ID-24-E at the Advanced Photon Source, Argonne National Laboratory. All measured diffraction spots were indexed, integrated and scaled using the XDS package (59).

The structure of GMPPNP-bound $KRAS^{G12R}$ was solved by molecular replacement using the program PHASER, based on the structure of GMPPNP-bound wild-type KRAS4B (60). The initial map showed interpretable electron density of the G-domain except for the switch regions. Further model improvement was performed with alternate rounds of refinement using Phenix.refine (61) and model building via COOT (62). Water molecules were included near the end of refinement. The majority of the model has a clear and well-interpretable electron density map with the exception of a few solvent-exposed side chains, which were omitted in the final model. The final data collection and refinement statistics are given in Extended Data Table S1. Figures were prepared using the program PyMOL.

Statistical Analysis

Data were analyzed by Graphpad Prism built-in test (One-Way Anova, Dunnet's multiple comparisons test). Data are presented relative to their respective control, or where noted in the figure legend, comparing the G12R condition to other conditions. For all graphs, error bars indicate mean ± s.e.m. for n≥3 independent experiments (except where noted) and p-values on graphs are denoted by ****P<0.0001, ***P<0.0002, **P<0.0021, *P<0.032, as determined in GraphPad Prism. Number of samples analyzed per experiment and whether data are representative or an average is indicated in the figure legend.

Supplementary Material

Refer to Web version on PubMed Central for supplementary material.

Acknowledgments

C.J.D. and A.D.C. were supported by grants from the National Cancer Institute (NCI) (R01CA42978, U01CA199235, P50CA196510, R35CA232113 and P01CA203657), the Department of Defense (W81XWH-15–1-0611) and the Lustgarten Pancreatic Cancer Foundation (388222). For C.J.D. and K.W., research was supported by the 2015 Pancreatic Cancer Action Network-AACR Research Acceleration Network Grant, Grant Number 15–90-25-DER. K.W. was supported by NCI P01CA203657. S.L.C. and E.F.P. were supported by NCI CA203657. A.J.A. was supported by Lustgarten Foundation, Dana-Farber Cancer Institute Hale Center for Pancreatic Cancer Research, the Doris Duke Charitable Foundation (2017066), Pancreatic Cancer Action Network (18–35-AGUI), NCI K08CA218420–02, P50CA127003, U01CA224146 (A.J.A). B.M.W. was supported by Lustgarten Foundation and DFCI Hale Family Center for Pancreatic Cancer Research. G.A.H. was supported by NCI F32CA200313 and

T32CA009156; N.M.B. by NCI F31CA180628; R.D.T., J.E.K. and C.M.G. by NCI T32CA009156. C.M.G. was supported by NCI F32CA221005. R.G.H. was supported by the 2018 Debbie's Dream Foundation-AACR Gastric Cancer Research Fellowship, in memory of Sally Mandel, Grant Number 18–40-41-HODG. A.M.W. was supported a fellowship from the American Cancer Society (PF-18–061); J.N.D. by NCI T32CA071341 and a fellowship from the Slomo and Cindy Silvian Foundation. A.M. and U.R. were supported by the Intramural Research Program of the NIH, NCI (ZIA BC 011267). B.P. was supported by the Deutsche Forschungsgemeinschaft (DFG PA 3051/1–1). K.L.B. was supported by T32CA009156 and by a Pancreatic Cancer Action Network/AACR Pathway to Leadership grant. Support to T.H.T., D.E. and D.K.S. was provided by NCI under contract HHSN261200800001E. Structural work used Northeastern Collaborative Access Team beamline (GM103403) at the Advanced Photon Source (DE-AC02–06CH11357). The UNC Microscopy Services Laboratory and Flow Cytometry Core Facility were supported in part by P30CA016086. Research reported in this publication was supported by the Center for AIDS Research award number 5P30AI050410. The content is solely the responsibility of the authors and does not necessarily represent the official views of the National Institutes of Health.

Disclosure of Potential Conflicts of Interests

C.J. Der is a consultant/advisory board member for Mirati Therapeutics and Deciphera Pharmaceuticals. C.J. Der has received research funding support from Mirati Therapeutics and Deciphera Pharmaceuticals. C.J. Der has consulted for Ribometrix, Jazz Therapeutics and Eli Lilly. A.D. Cox has consulted for Eli Lilly and Mirati Therapeutics. A.J. Aguirre has consulted for Oncorus, Inc., Arrakis Therapeutics and Merck & Co., Inc. A.J. Aguirre has received research funding support from Mirati Therapeutics and Deerfield, Inc. B.M. Wolpin has consulted for BioLineRx, Celgene, G1 Therapeutics and GRAIL. B.M. Wolpin has received research funding support from Celgene and Eli Lilly.

REFERENCES

1. Cox AD, Fesik SW, Kimmelman AC, Luo J, Der CJ. Drugging the undruggable RAS: mission possible? Nature reviews Drug discovery 2014;13:828–51. [PubMed: 25323927]
2. Papke B, Der CJ. Drugging RAS: Know the enemy. Science 2017;355:1158–63. [PubMed: 28302824]
3. AMG 510 First to Inhibit "Undruggable" KRAS. Cancer Discov 2019;9:988–9.
4. Haigis KM. KRAS alleles: the devil is in the detail. Trends Cancer 2017;3:686–97. [PubMed: 28958387]
5. Waters AM, Der CJ. KRAS: the critical driver and therapeutic target for pancreatic cancer. Cold Spring Harb Perspect Med 2017.
6. Network. CGAR. Integrated genomic characterization of pancreatic ductal adenocarcinoma. Cancer Cell 2017;32:185–203 e13. [PubMed: 28810144]
7. Gupta S, Ramjaun AR, Haiko P, Wang Y, Warne PH, Nicke B, et al. Binding of ras to phosphoinositide 3-kinase p110alpha is required for ras-driven tumorigenesis in mice. Cell 2007;129:957–68. [PubMed: 17540175]
8. Kamphorst JJ, Nofal M, Commisso C, Hackett SR, Lu W, Grabocka E, et al. Human pancreatic cancer tumors are nutrient poor and tumor cells actively scavenge extracellular protein. Cancer research 2015;75:544–53. [PubMed: 25644265]
9. Bryant KL, Mancias JD, Kimmelman AC, Der CJ. KRAS: feeding pancreatic cancer proliferation. Trends in biochemical sciences 2014;39:91–100. [PubMed: 24388967]
10. Commisso C, Davidson SM, Soydaner-Azeloglu RG, Parker SJ, Kamphorst JJ, Hackett S, et al. Macropinocytosis of protein is an amino acid supply route in Ras-transformed cells. Nature 2013;497:633–7. [PubMed: 23665962]
11. Hayes TK, Neel NF, Hu C, Gautam P, Chenard M, Long B, et al. Long-Term ERK inhibition in KRAS-mutant pancreatic cancer is associated with MYC degradation and senescence-like growth suppression. Cancer Cell 2016;29:75–89. [PubMed: 26725216]
12. Campbell PM, Groehler AL, Lee KM, Ouellette MM, Khazak V, Der CJ. K-Ras promotes growth transformation and invasion of immortalized human pancreatic cells by Raf and phosphatidylinositol 3-kinase signaling. Cancer research 2007;67:2098–106. [PubMed: 17332339]
13. Oldham SM, Clark GJ, Gangarosa LM, Coffey RJ Jr., Der CJ. Activation of the Raf-1/MAP kinase cascade is not sufficient for Ras transformation of RIE-1 epithelial cells. Proc Natl Acad Sci U S A 1996;93:6924–8. [PubMed: 8692920]

14. Shao DD, Xue W, Krall EB, Bhutkar A, Piccioni F, Wang X, et al. KRAS and YAP1 converge to regulate EMT and tumor survival. Cell 2014;158:171–84. [PubMed: 24954536]
15. Hunter JC, Manandhar A, Carrasco MA, Gurbani D, Gondi S, Westover KD. Biochemical and Structural Analysis of Common Cancer-Associated KRAS Mutations. Mol Cancer Res 2015;13:1325–35. [PubMed: 26037647]
16. Krengel U, Schlichting I, Scherer A, Schumann R, Frech M, John J, et al. Three-dimensional structures of H-ras p21 mutants: molecular basis for their inability to function as signal switch molecules. Cell 1990;62:539–48. [PubMed: 2199064]
17. Smith MJ, Neel BG, Ikura M. NMR-based functional profiling of RASopathies and oncogenic RAS mutations. Proc Natl Acad Sci U S A 2013;110:4574–9. [PubMed: 23487764]
18. Iwig JS, Vercoulen Y, Das R, Barros T, Limnander A, Che Y, et al. Structural analysis of autoinhibition in the Ras-specific exchange factor RasGRP1. Elife 2013;2:e00813. [PubMed: 23908768]
19. Mott HR, Owen D. Structures of Ras superfamily effector complexes: What have we learnt in two decades? Crit Rev Biochem Mol Biol 2015;50:85–133. [PubMed: 25830673]
20. Welsch ME, Kaplan A, Chambers JM, Stokes ME, Bos PH, Zask A, et al. Multivalent small-molecule pan-RAS inhibitors. Cell 2017;168:878–89 e29. [PubMed: 28235199]
21. Pacold ME, Suire S, Perisic O, Lara-Gonzalez S, Davis CT, Walker EH, et al. Crystal structure and functional analysis of Ras binding to its effector phosphoinositide 3-kinase gamma. Cell 2000;103:931–43. [PubMed: 11136978]
22. Khosravi-Far R, White MA, Westwick JK, Solski PA, Chrzanowska-Wodnicka M, Van Aelst L, et al. Oncogenic Ras activation of Raf/mitogen-activated protein kinase-independent pathways is sufficient to cause tumorigenic transformation. Mol Cell Biol 1996;16:3923–33. [PubMed: 8668210]
23. White MA, Nicolette C, Minden A, Polverino A, Van Aelst L, Karin M, et al. Multiple Ras functions can contribute to mammalian cell transformation. Cell 1995;80:533–41. [PubMed: 7867061]
24. Rodriguez-Viciana P, Warne PH, Khwaja A, Marte BM, Pappin D, Das P, et al. Role of phosphoinositide 3-OH kinase in cell transformation and control of the actin cytoskeleton by Ras. Cell 1997;89:457–67. [PubMed: 9150145]
25. Federici G, Gao X, Slawek J, Arodz T, Shitaye A, Wulfkuhle JD, et al. Systems analysis of the NCI-60 cancer cell lines by alignment of protein pathway activation modules with “-OMIC” data fields and therapeutic response signatures. Mol Cancer Res 2013;11:676–85. [PubMed: 23635402]
26. Hoeller O, Bolourani P, Clark J, Stephens LR, Hawkins PT, Weiner OD, et al. Two distinct functions for PI3-kinases in macropinocytosis. J Cell Sci 2013;126:4296–307. [PubMed: 23843627]
27. Herrmann C, Martin GA, Wittinghofer A. Quantitative analysis of the complex between p21ras and the Ras-binding domain of the human Raf-1 protein kinase. J Biol Chem 1995;270:2901–5. [PubMed: 7852367]
28. McFall A, Ulku A, Lambert QT, Kusa A, Rogers-Graham K, Der CJ. Oncogenic Ras blocks anoikis by activation of a novel effector pathway independent of phosphatidylinositol 3-kinase. Mol Cell Biol 2001;21:5488–99. [PubMed: 11463831]
29. Ying H, Kimmelman AC, Lyssiotis CA, Hua S, Chu GC, Fletcher-Sananikone E, et al. Oncogenic Kras maintains pancreatic tumors through regulation of anabolic glucose metabolism. Cell 2012;149:656–70. [PubMed: 22541435]
30. Vaseva AV, Blake DR, Gilbert TSK, Ng S, Hostetter G, Azam SH, et al. KRAS Suppression-Induced Degradation of MYC Is Antagonized by a MEK5-ERK5 Compensatory Mechanism. Cancer Cell 2018;34:807–22. [PubMed: 30423298]
31. Fabregat A, Jupe S, Matthews L, Sidiropoulos K, Gillespie M, Garapati P, et al. The Reactome Pathway Knowledgebase. Nucleic Acids Res 2018;46:D649–D55. [PubMed: 29145629]
32. Vanhaesebroeck B, Guillermet-Guibert J, Graupera M, Bilanges B. The emerging mechanisms of isoform-specific PI3K signalling. Nat Rev Mol Cell Biol 2010;11:329–41. [PubMed: 20379207]

33. Baer R, Cintas C, Dufresne M, Cassant-Sourdy S, Schonhuber N, Planque L, et al. Pancreatic cell plasticity and cancer initiation induced by oncogenic Kras is completely dependent on wild-type PI 3-kinase p110alpha. Genes Dev 2014;28:2621–35. [PubMed: 25452273]
34. Welch HC, Coadwell WJ, Ellson CD, Ferguson GJ, Andrews SR, Erdjument-Bromage H, et al. P-Rex1, a PtdIns(3,4,5)P3- and Gbetagamma-regulated guanine-nucleotide exchange factor for Rac. Cell 2002;108:809–21. [PubMed: 11955434]
35. Yao W, Rose JL, Wang W, Seth S, Jiang H, Taguchi A, et al. Syndecan 1 is a critical mediator of macropinocytosis in pancreatic cancer. Nature 2019;568:410–4. [PubMed: 30918400]
36. Fujii M, Kawai K, Egami Y, Araki N. Dissecting the roles of Rac1 activation and deactivation in macropinocytosis using microscopic photo-manipulation. Sci Rep 2013;3:2385. [PubMed: 23924974]
37. Ryan MB, Der CJ, Wang-Gillam A, Cox AD. Targeting RAS-mutant cancers: is ERK the key? Trends Cancer 2015;1:183–98. [PubMed: 26858988]
38. Bryant KL, Stalnecker CA, Zeitouni D, Klomp JE, Peng S, Tikunov AP, et al. Combination of ERK and autophagy inhibition as a treatment approach for pancreatic cancer. Nat Med 2019;25:628–40. [PubMed: 30833752]
39. Bournet B, Muscari F, Buscail C, Assenat E, Barthet M, Hammel P, et al. KRAS G12D mutation subtype is a prognostic factor for advanced pancreatic adenocarcinoma. Clin Transl Gastroenterol 2016;7:e157. [PubMed: 27010960]
40. Castellano E, Downward J. RAS Interaction with PI3K: More Than Just Another Effector Pathway. Genes Cancer 2011;2:261–74. [PubMed: 21779497]
41. Poulin EJ, Bera AK, Lu J, Lin YJ, Strasser SD, Paulo JA, et al. Tissue-Specific Oncogenic Activity of KRAS(A146T). Cancer Discov 2019;9:738–55. [PubMed: 30952657]
42. Winters IP, Chiou SH, Paulk NK, McFarland CD, Lalgudi PV, Ma RK, et al. Multiplexed in vivo homology-directed repair and tumor barcoding enables parallel quantification of Kras variant oncogenicity. Nat Commun 2017;8:2053. [PubMed: 29233960]
43. Castellano E, Sheridan C, Thin MZ, Nye E, Spencer-Dene B, Diefenbacher ME, et al. Requirement for interaction of PI3-kinase p110alpha with RAS in lung tumor maintenance. Cancer Cell 2013;24:617–30. [PubMed: 24229709]
44. Boj SF, Hwang CI, Baker LA, Chio II, Engle DD, Corbo V, et al. Organoid models of human and mouse ductal pancreatic cancer. Cell 2015;160:324–38. [PubMed: 25557080]
45. Tiriac H, Belleau P, Engle DD, Plenker D, Deschenes A, Somerville TDD, et al. Organoid Profiling Identifies Common Responders to Chemotherapy in Pancreatic Cancer. Cancer Discov 2018;8:1112–29. [PubMed: 29853643]
46. Baldelli E, Calvert V, Hodge A, VanMeter A, Petricoin EF 3rd, Pierobon M. Reverse phase protein microarrays. Methods Mol Biol 2017;1606:149–69. [PubMed: 28502000]
47. Pin E, Federici G, Petricoin EF 3rd. Preparation and use of reverse protein microarrays. Curr Protoc Protein Sci 2014;75:Unit 27 7.
48. Pin E, Stratton S, Belluco C, Liotta L, Nagle R, Hodge KA, et al. A pilot study exploring the molecular architecture of the tumor microenvironment in human prostate cancer using laser capture microdissection and reverse phase protein microarray. Mol Oncol 2016;10:1585–94. [PubMed: 27825696]
49. Signore M, Reeder KA. Antibody validation by Western blotting. Methods Mol Biol 2012;823:139–55. [PubMed: 22081344]
50. Baldelli E, Bellezza G, Haura EB, Crino L, Cress WD, Deng J, et al. Functional signaling pathway analysis of lung adenocarcinomas identifies novel therapeutic targets for KRAS mutant tumors. Oncotarget 2015;6:32368–79. [PubMed: 26468985]
51. Pemovska T, Kontro M, Yadav B, Edgren H, Eldfors S, Szwajda A, et al. Individualized systems medicine strategy to tailor treatments for patients with chemorefractory acute myeloid leukemia. Cancer Discov 2013;3:1416–29. [PubMed: 24056683]
52. Scheich C, Kummel D, Soumailakakis D, Heinemann U, Bussow K. Vectors for co-expression of an unrestricted number of proteins. Nucleic Acids Res 2007;35:e43. [PubMed: 17311810]
53. Smith MJ, Ikura M. Integrated RAS signaling defined by parallel NMR detection of effectors and regulators. Nat Chem Biol 2014;10:223–30. [PubMed: 24441586]

54. Bunney TD, Harris R, Gandarillas NL, Josephs MB, Roe SM, Sorli SC, et al. Structural and mechanistic insights into ras association domains of phospholipase C epsilon. Molecular cell 2006;21:495–507. [PubMed: 16483931]

55. Jaiswal BS, Janakiraman V, Kljavin NM, Chaudhuri S, Stern HM, Wang W, et al. Somatic mutations in p85alpha promote tumorigenesis through class IA PI3K activation. Cancer Cell 2009;16:463–74. [PubMed: 19962665]

56. Wakizaka A, Kurosaka K, Okuhara E. Rapid separation of DNA constituents, bases, nucleosides and nucleotides, under the same chromatographic conditions using high-performance liquid chromatography with a reversed-phase column. J Chromatogr 1979;162:319–26. [PubMed: 528598]

57. Lenzen C, Cool RH, Wittinghofer A. Analysis of intrinsic and CDC25-stimulated guanine nucleotide exchange of p21ras-nucleotide complexes by fluorescence measurements. Methods Enzymol 1995;255:95–109. [PubMed: 8524141]

58. Block C, Janknecht R, Herrmann C, Nassar N, Wittinghofer A. Quantitative structure-activity analysis correlating Ras/Raf interaction in vitro to Raf activation in vivo. Nat Struct Biol 1996;3:244–51. [PubMed: 8605626]

59. Xds Kabsch W. Acta Crystallogr D Biol Crystallogr 2010;66:125–32. [PubMed: 20124692]

60. McCoy AJ, Grosse-Kunstleve RW, Adams PD, Winn MD, Storoni LC, Read RJ. Phaser crystallographic software. J Appl Crystallogr 2007;40:658–74. [PubMed: 19461840]

61. Adams PD, Afonine PV, Bunkoczi G, Chen VB, Davis IW, Echols N, et al. PHENIX: a comprehensive Python-based system for macromolecular structure solution. Acta Crystallogr D Biol Crystallogr 2010;66:213–21. [PubMed: 20124702]

62. Emsley P, Lohkamp B, Scott WG, Cowtan K. Features and development of Coot. Acta Crystallogr D Biol Crystallogr 2010;66:486–501. [PubMed: 20383002]

SIGNIFICANCE

We determined that $KRAS^{G12R}$ is impaired in activating a key effector, p110α phosphoinositide 3-kinase. As such, $KRAS^{G12R}$ is impaired in driving macropinocytosis. However, overexpression of PI3Kγ in PDAC compensates for this deficiency, providing one basis for the prevalence of this otherwise rare KRAS mutant in pancreatic but not other cancers.

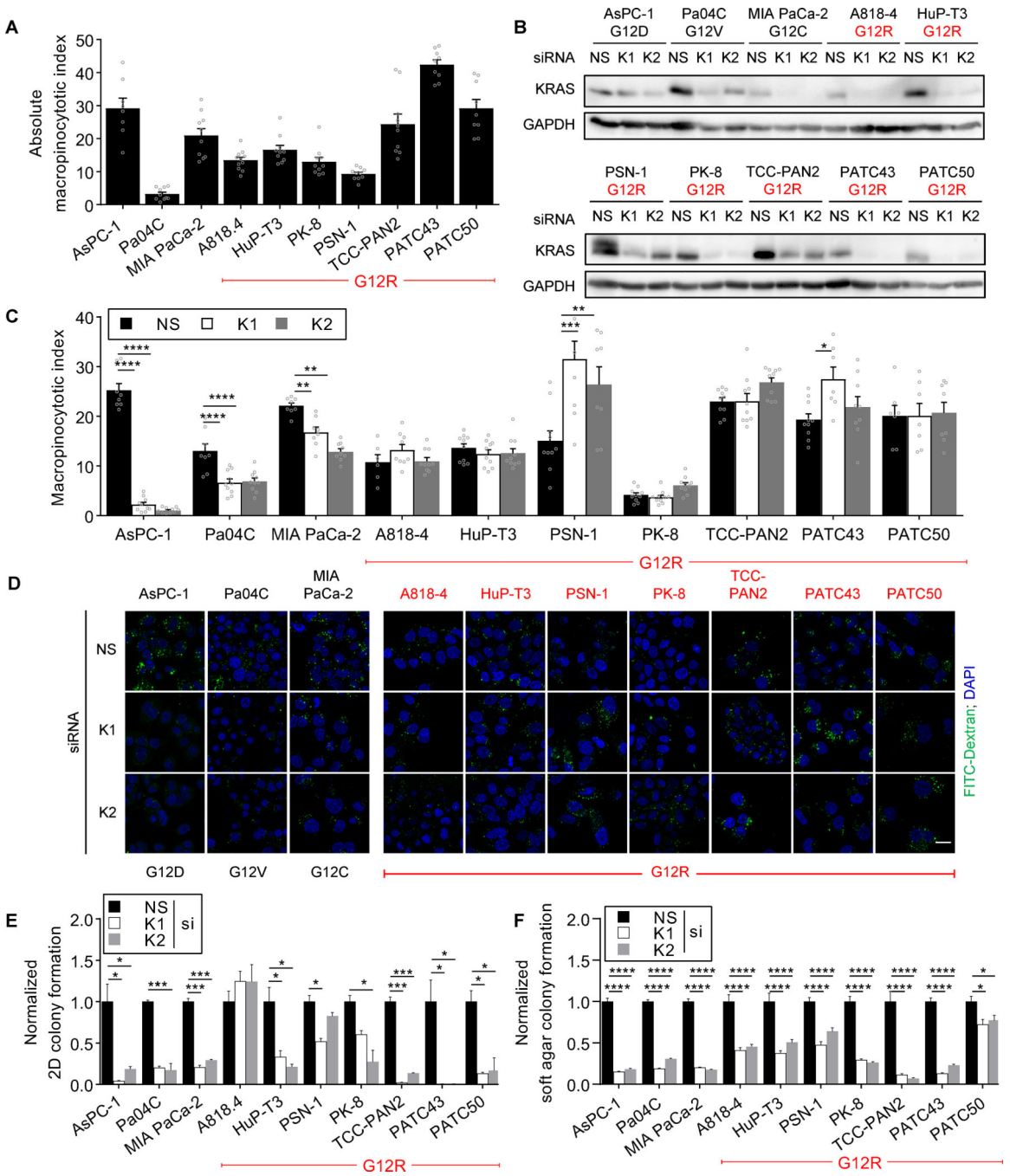

Figure 1.

KRAS-independent macropinocytosis in KRAS^{G12R}-mutant PDAC cell lines. **A**, Quantification of FITC-dextran-labeled macropinosomes in PDAC cell lines. Data shown are representative of three independent experiments. All FITC-dextran experiments analyzed at least 75 cells in approximately 10 randomly selected fields of view per condition. **B**, Immunoblot analysis of KRAS expression upon silencing using a nonspecific (NS) and two *KRAS*-targeting siRNAs. **C**, Quantification of FITC-dextran-labeled macropinosomes in KRAS siRNA-silenced PDAC cell lines. Data shown are representative of three independent

experiments and normalized to the corresponding NS treatment, unless indicated otherwise. **D**, Representative images of FITC-dextran-labeled macropinosomes from **C**. Macropinosomes were labeled by exposure with FITC-dextran (green) and nuclei stained by DAPI (blue). **E**, Anchorage-dependent colony formation of PDAC treated with *KRAS* siRNA. Cells were cultured for seven days and developed with crystal violet. Data are the average of six replicates. **F**, Anchorage-independent colony formation of PDAC treated with KRAS siRNA. Cells were cultured for seven days and developed with AlamarBlue reagent. Data are the average of six replicates. **** $P<0.0001$, *** $P<0.0002$, ** $P<0.0021$, * $P<0.032$, p values from Dunnett's multiple comparison test after one-way ANOVA, comparing K1/K2 lanes to respective NS controls. Scale bar, 20 μm. Error bars, mean ± s.e.m.

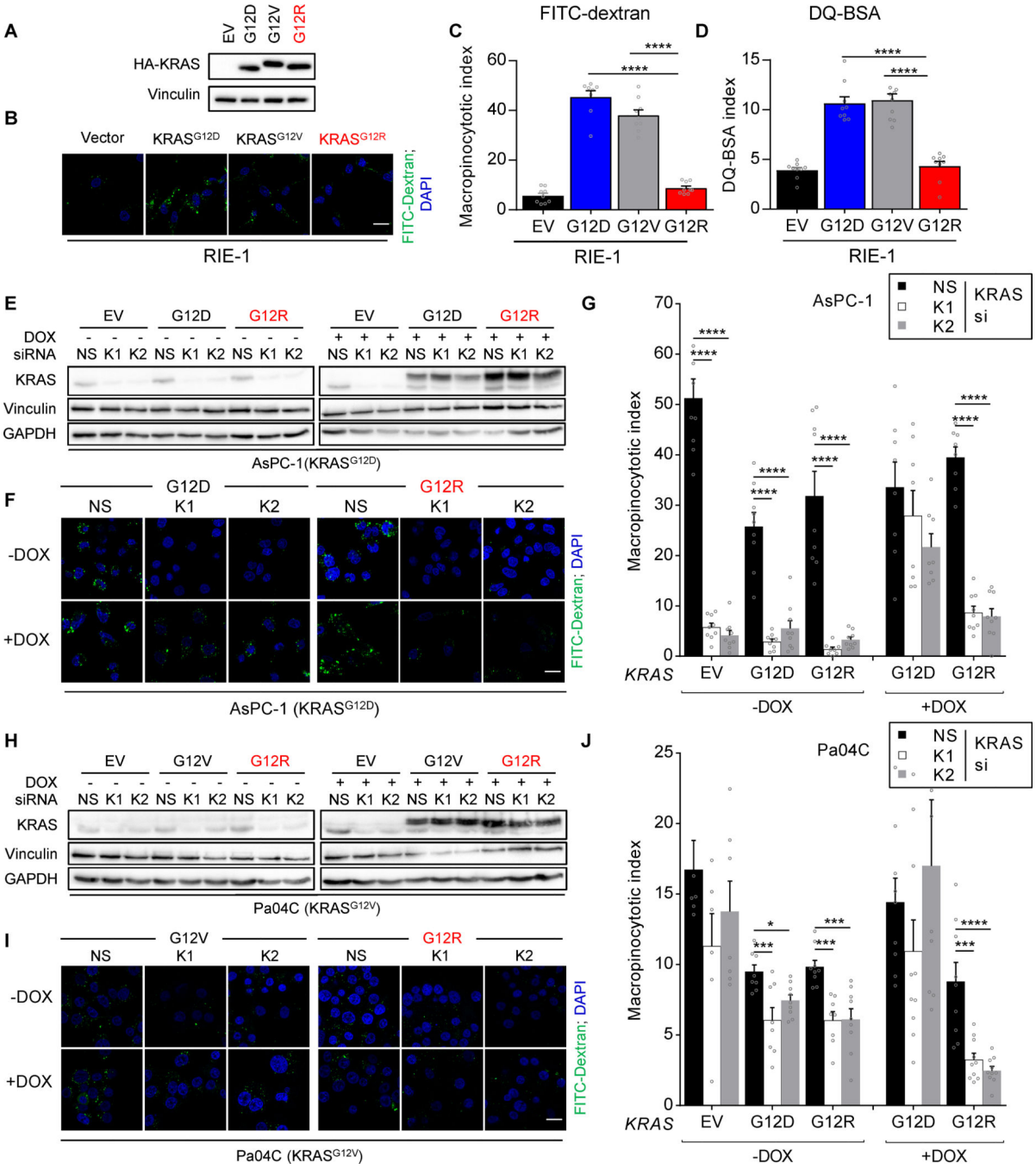

Figure 2.

Exogenous KRAS^{G12D} but not KRAS^{G12R} rescues KRAS-dependent macropinocytosis. **A**, Immunoblot analysis of HA epitope-tagged KRAS mutant proteins stably expressed in RIE-1 cells. **B**, FITC-dextran-labeled macropinosomes in KRAS-transformed RIE-1 cells. Macropinosomes, green; nuclei, blue. **C**, Quantification of FITC-dextran uptake in RIE-1 cells. Mean values plotted with each data point representing one field and at least 75 cells per condition were analyzed. Data are representative of at least 3 independent experiments **D**, Quantification of DQ-BSA in macropinosomes of RIE-1 cells, as in **B**; data are

representative of at least three independent experiments. P values from Dunnett's multiple comparison test after one-way ANOVA, comparing all conditions to G12R. **E**, Immunoblot analysis of AsPC-1 cells expressing doxycycline-inducible HA-KRAS mutant proteins with or without siRNA silencing of *KRAS*. **F**, FITC-dextran-labeled macropinosomes in AsPC-1 cells. Macropinosomes, green; nuclei, blue. **G**, Quantification of FITC-dextran uptake in AsPC-1 cells, as in **B**. **H**, Immunoblot analysis of Pa04C cells expressing doxycycline-inducible HA-KRAS mutant proteins with or without siRNA silencing of *KRAS*. **I**, FITC-dextran-labeled macropinosomes in Pa04C cells. Macropinosomes, green; nuclei, blue. **J**, Quantification of FITC-dextran uptake in Pa04C cells, as in **B**. Data are representative of three independent experiments for AsPC-1 cells and two for Pa04C cells. ****P<0.0001, ***P<0.0002, *P<0.032, p values from Dunnett's multiple comparison test after one-way ANOVA, comparing K1/K2 lanes to respective NS controls. Scale bar, 20 μm. Error bars, mean ± s.e.m.

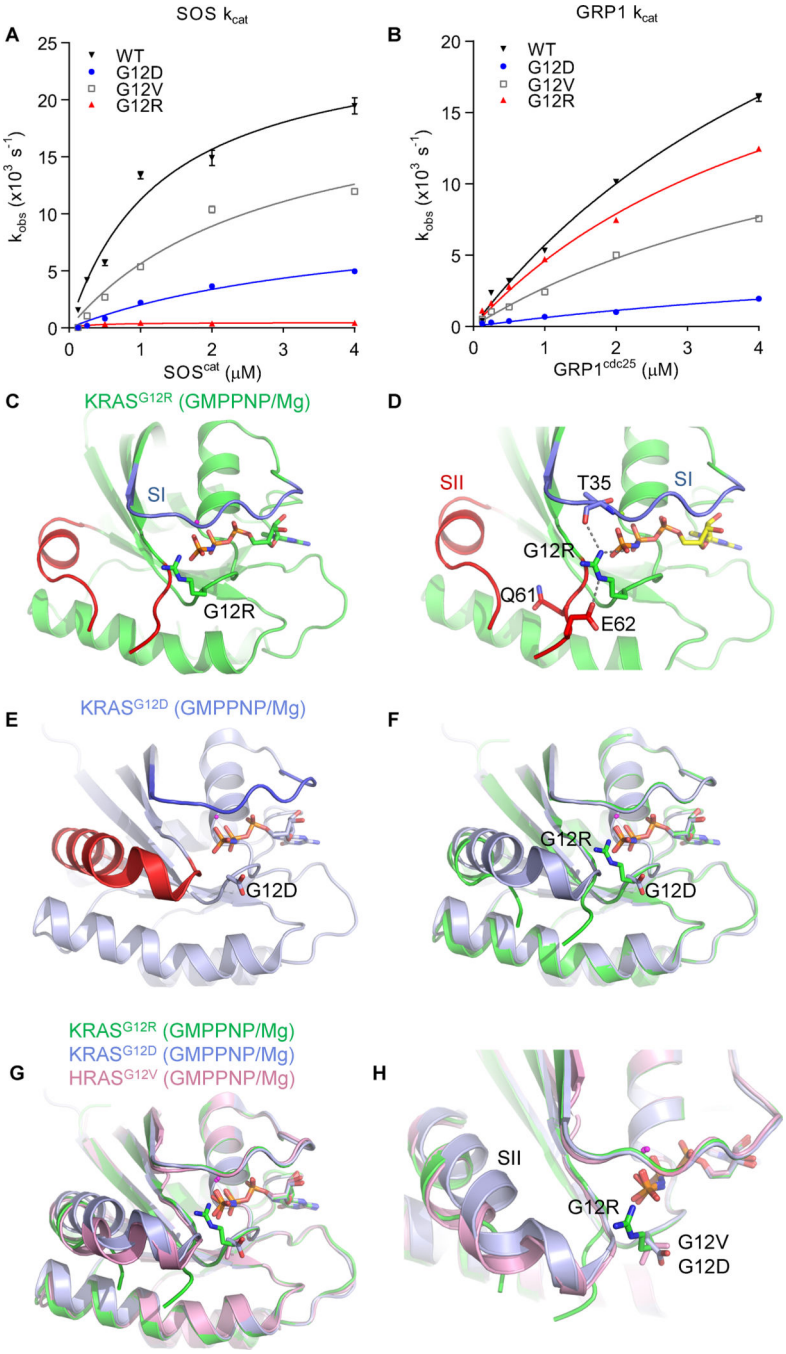

Figure 3.

KRAS^{G12R} is insensitive to SOS^{cat} and has an altered switch II structure. **A**, Measurement of the k_{cat} of SOS1-mediated nucleotide exchange. **B,** Measurement of the k_{cat} of GRP1-mediated nucleotide exchange. Data are the average of three independent experiments. Error bars, mean ± s.e.m. **C,** Ribbon diagram of the crystal structure of KRAS^{G12R}; PDB 6CU6. Switch I (SI), blue; switch II (SII), red. The nucleotide analog GMPPNP and arginine (G12R) are drawn as sticks. **D,** Magnification of the nucleotide binding pocket in KRAS^{G12R}. Dotted lines represent hydrogen bonds. Nitrogen, dark blue; oxygen, light red;

phosphate, orange. **E,** $KRAS^{G12D}$ (PDB 5USJ) crystal structure shown for reference. Coloring is the same as in panel **B**. **F,** Overlay of $KRAS^{G12R}$ (green) and $KRAS^{G12D}$ (blue) ribbon diagrams. **G,** Overlay of ribbon diagrams of $KRAS^{G12R}$ (green), $KRAS^{G12D}$ (blue) and $HRAS^{G12V}$ (pink, PDB 1HE8). **H**, Magnification of the nucleotide binding pocket. Mutant sidechains are drawn as sticks for reference.

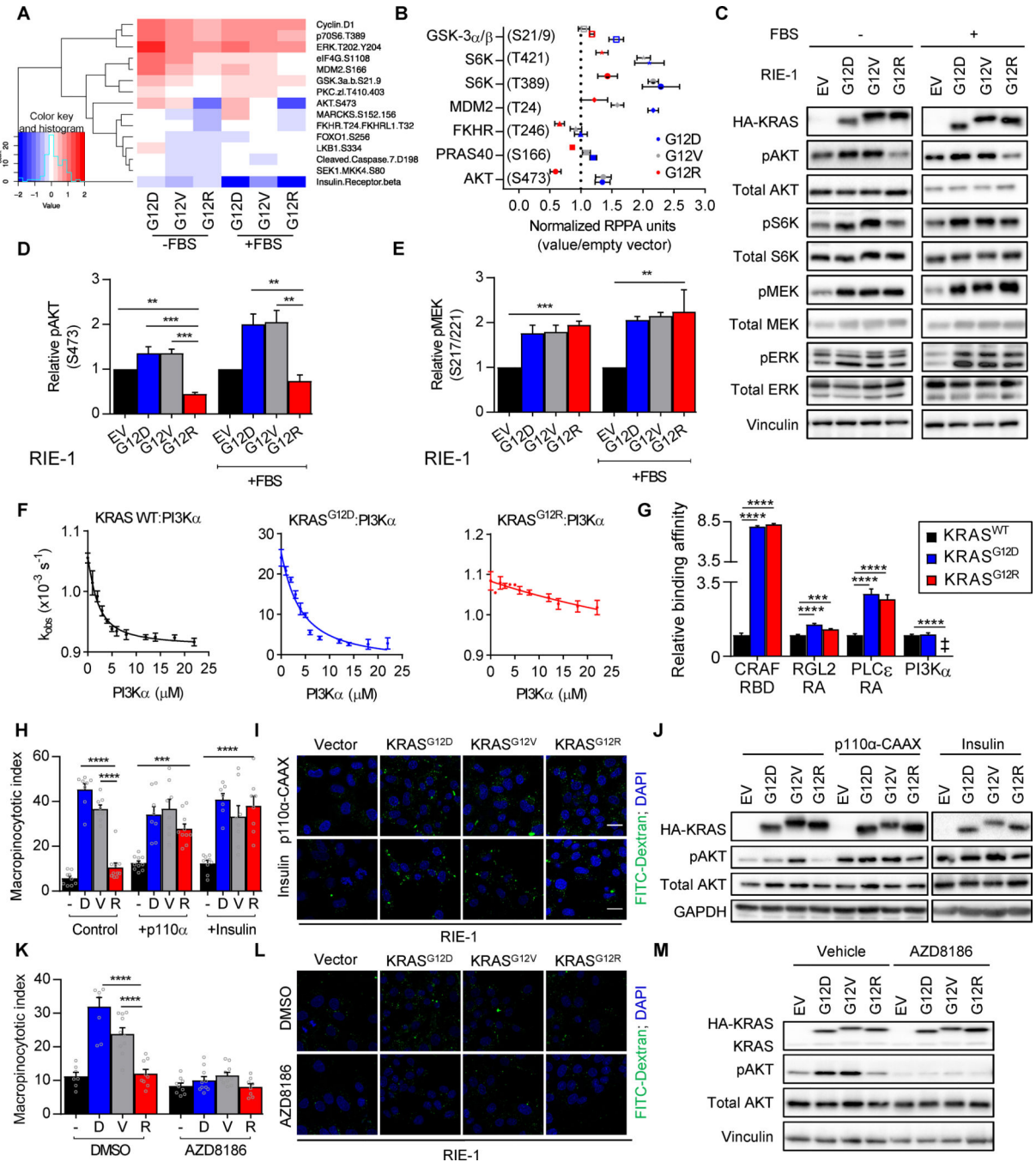

Figure 4.

KRAS^{G12R} fails to drive macropinocytosis due to loss of PI3Kα activation. **A**, Heatmap of the relative RPPA intensities in RIE-1 cells ectopically expressing KRAS mutants. Phosphosites depicted had a *P*-value <0.1 by Student's *t*-test comparing G12D to G12R in serum-free conditions. **B**, RPPA intensities of select protein features, normalized to empty vector. Data are the average of three independent experiments. **C,** Immunoblot analysis of RIE-1 cells stably expressing HA-KRAS mutant proteins in the absence or presence of serum. Data are representative of three independent experiments. **D**, Quantification of

phosphorylation of AKT S473 and **E**, MEK S217/221 in KRAS-transformed RIE-1 cells. Data are an average of three independent experiments. P values from Dunnett's multiple comparison test after one-way ANOVA, comparing all lanes to G12R for each condition. **F**, *In vitro* measurement of KRAS:PI3Kα binding using the inhibition of nucleotide dissociation assay. **G**, Normalized *in vitro* binding affinity measurements of KRAS proteins to the RBD/RA domains of RAS effectors and full-length PI3Kα. Binding was normalized to KRAS WT for each effector. ‡ No binding detected. P values from Dunnett's multiple comparison test after one-way ANOVA, comparing each lane to WT. Data are an average of three independent experiments. **H**, Quantification of FITC-dextran-labeled macropinosomes in RIE-1 cells expressing HA epitope-tagged KRAS mutants with constitutively activated p110α-CAAX or after addition of insulin to the medium. P values from Dunnett's multiple comparison test after one-way ANOVA, comparing each lane to G12R. **I**, Representative images of cells quantified in **H**. Macropinosomes, green; nuclei, blue. **J**, Immunoblot analysis cells from panel **H**. Data are representative of three independent experiments. **K**, Quantification of FITC-dextran-labeled macropinosomes in RIE-1 cells expressing HA-KRAS mutants treated with the p110α/β/δ inhibitor AZD8186 (1 μM, 48 h). **L**, Representative images of cells quantified in **K**. **M**, Immunoblot analysis cells from panel **K**. P values from Dunnett's multiple comparison test after one-way ANOVA, comparing all lanes to G12R for each treatment. Data are representative of three independent experiments. **** $P<0.0001$, *** $P<0.0002$, ** $P<0.0021$; Mean values plotted, with each data point representing one field and at least 75 cells per condition. Scale bar, 20 μm. Error bars, mean ± s.e.m.

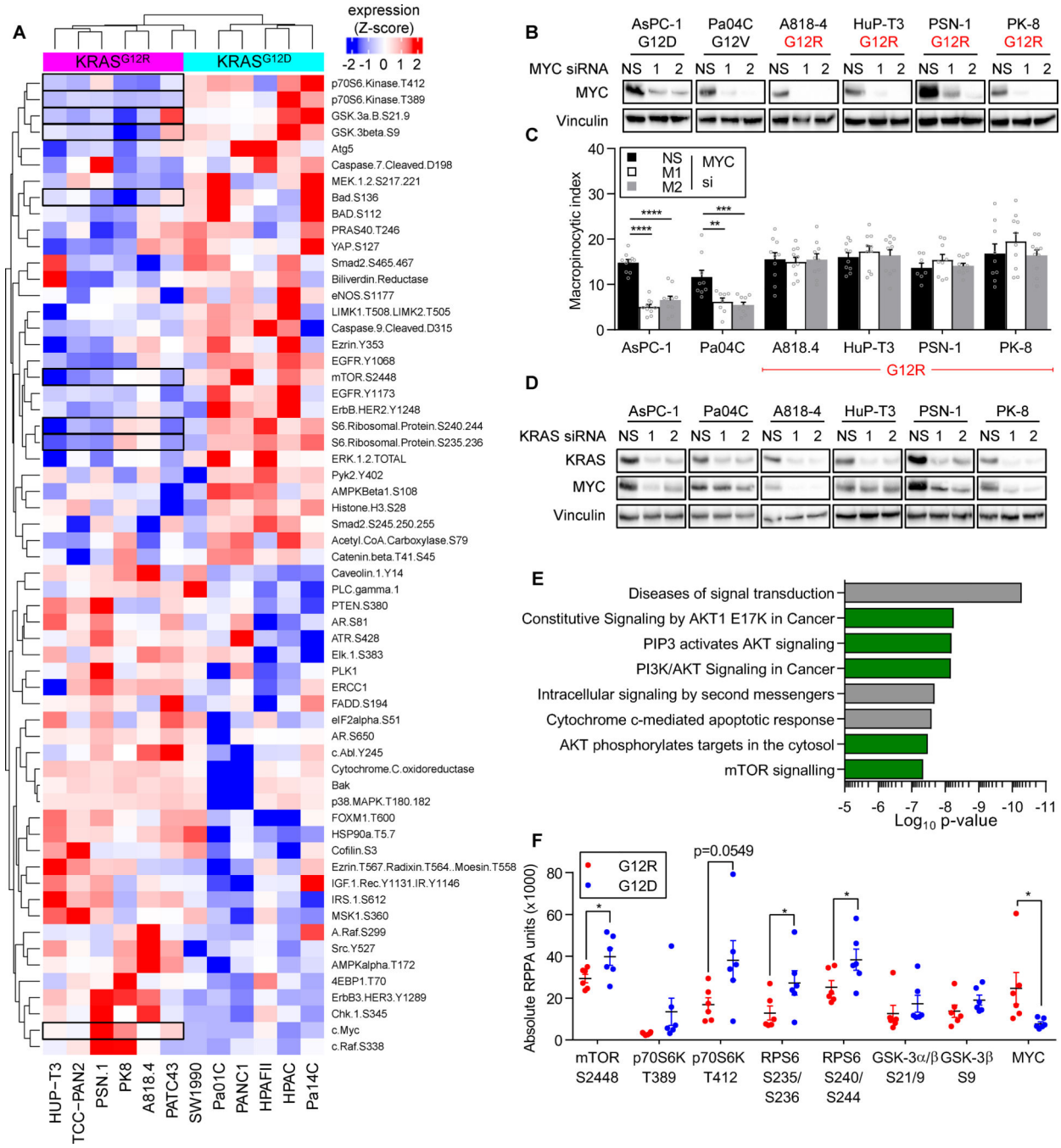

Figure 5.

KRAS^{G12R}-mutant PDAC cell lines have a distinct cell signaling profile. **A**, RPPA analysis of six *KRAS*^{G12R} PDAC cell lines and seven *KRAS*$^{G12D/V}$ PDAC cell lines under basal growth conditions. The top and bottom 30 features most differentially expressed between the two mutational groups are shown. Selected features are highlighted. **B**, Immunoblot analysis of PDAC cell lines after 48 h of *MYC* siRNA treatment. **C,** Quantification of FITC-dextran uptake after 48 h of *MYC* siRNA treatment. Mean values plotted, with each data point representing one field and at least 75 cells per condition. P values from Dunnett's multiple

comparison test after one-way ANOVA, comparing the K1/K2 lanes to the respective NS controls. **** $P<0.0001$, ** $P<0.0021$; Error bars, mean ± s.e.m. **D,** Immunoblot analysis of PDAC cell lines treated with siRNA to silence *KRAS*. **E**, Reactome2016 profiling of the 30 protein features that were most decreased in the $KRAS^{G12R}$ PDAC cell lines. **F**, Dot plot of selected phosphorylated and total proteins from the RPPA data. Cell lines were grouped into $KRAS^{G12R}$ or non-$KRAS^{G12R}$ and the median value from three independent experiments for each cell line was plotted. *P<0.05, p values from a two-tailed unpaired *t*-test for each protein.

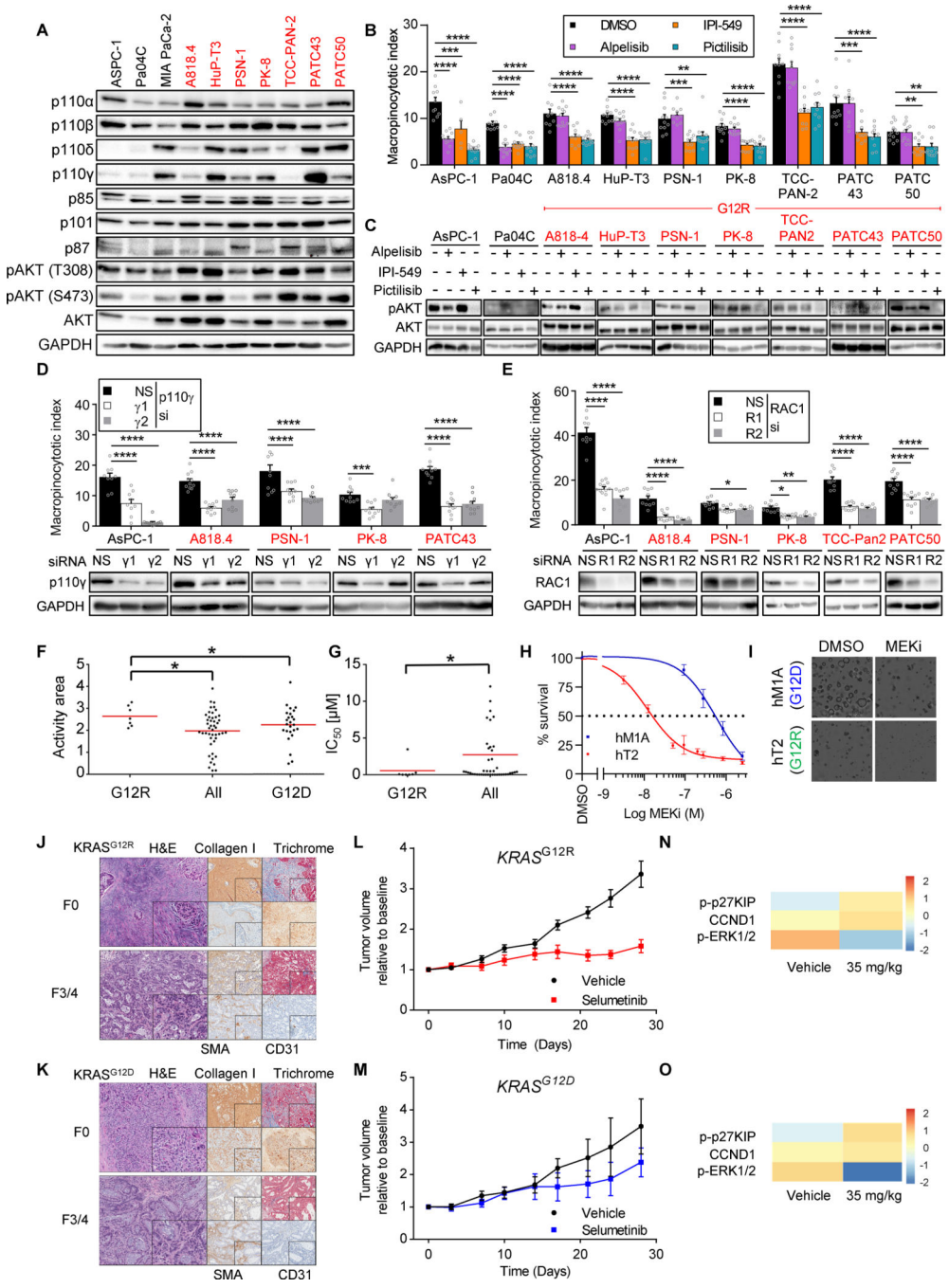

Figure 6.

KRAS^{G12R}-mutant PDAC rely on p110γ for macropinocytosis and are more sensitive than KRAS^{G12D}-mutant PDAC to MEK/ERK inhibition. **A**, Immunoblot analysis of p110 isoforms in PDAC. **B,** Quantification of FITC-dextran-labeled macropinosomes in PDAC cell lines treated with DMSO, alpelisib (p110α-selective inhibitor, 100 nM), IPI-549 (p110γ-selective inhibitor, 300 nM) or pictilisib (pan-p110 inhibitor, 1.5 μM) for 18 h. Data are representative of four independent experiments. **C**, Immunoblot analysis of cells from **B**. **D**, Quantification of FITC-dextran labeled macropinosomes after 72 h of *PIK3CG* siRNA

treatment. Immunoblot analysis below. Data are representative of three independent experiments. **E**, Quantification of FITC-dextran labeled macropinosomes after 72 h of *RAC1* siRNA treatment. Immunoblot analysis below. Data are representative of three independent experiments. Mean values plotted, with each data point representing one field and at least 75 cells per condition. P values from Dunnett's multiple comparison test after one-way ANOVA, comparing all treatments to DMSO or NS. ****P<0.0001, ***P<0.0002, **P<0.0021, *P<0.032, Error bars, mean ± s.e.m. **F**, Scatter plot of average activity (AA) area and **G**, individual IC_{50} values of $KRAS^{G12R}$ vs. non-$KRAS^{G12R}$ lines. Whitney Mann U-test, 2-tailed; *p<0.05. **H**, Cell viability of PDAC organoid cultures treated with MEKi (selumetinib). Organoids were cultured for 10 days. Data are the average of four independent experiments. **I**, Bright field images from **H**. **J**, Cytoarchitecture of $KRAS^{G12R}$-mutant pancreas cancer PDX. F0, prior to xenotransplantation, F3/4, after 3–4 passages in NOD/SCID mice. Left, H&E; right, immunohistochemical stains for collagen I, anti-smooth muscle antigen (SMA), anti-CD31 and trichrome (20x). **K**, Cytoarchitecture of $KRAS^{G12D}$-mutant pancreas cancer PDX, as in **J**. **L**, Tumor volume of patient-derived pancreatic tumors expressing $KRAS^{G12R}$ in immunocompromised NOD/SCID mice treated with MEKi. When tumor volume reached 200 mm^3, MEKi (35 mg/kg) was given twice daily by oral gavage. Bi-weekly tumor measurements (n≥10 animals per arm) were normalized to tumor volume at the start of treatment. Error bars, mean ± s.e.m. **M**, Tumor volume of patient-derived pancreatic tumors expressing $KRAS^{G12D}$ treated with MEKi, as in **L**. **N**, RPPA analysis of $KRAS^{G12R}$-expressing tumors excised after 28 days of treatment (mean of 4 tumors). Protein signals were normalized to total protein, levels shown as log2-transformed measures. **O**, RPPA analysis of $KRAS^{G12D}$-expressing tumors, as in **N**.

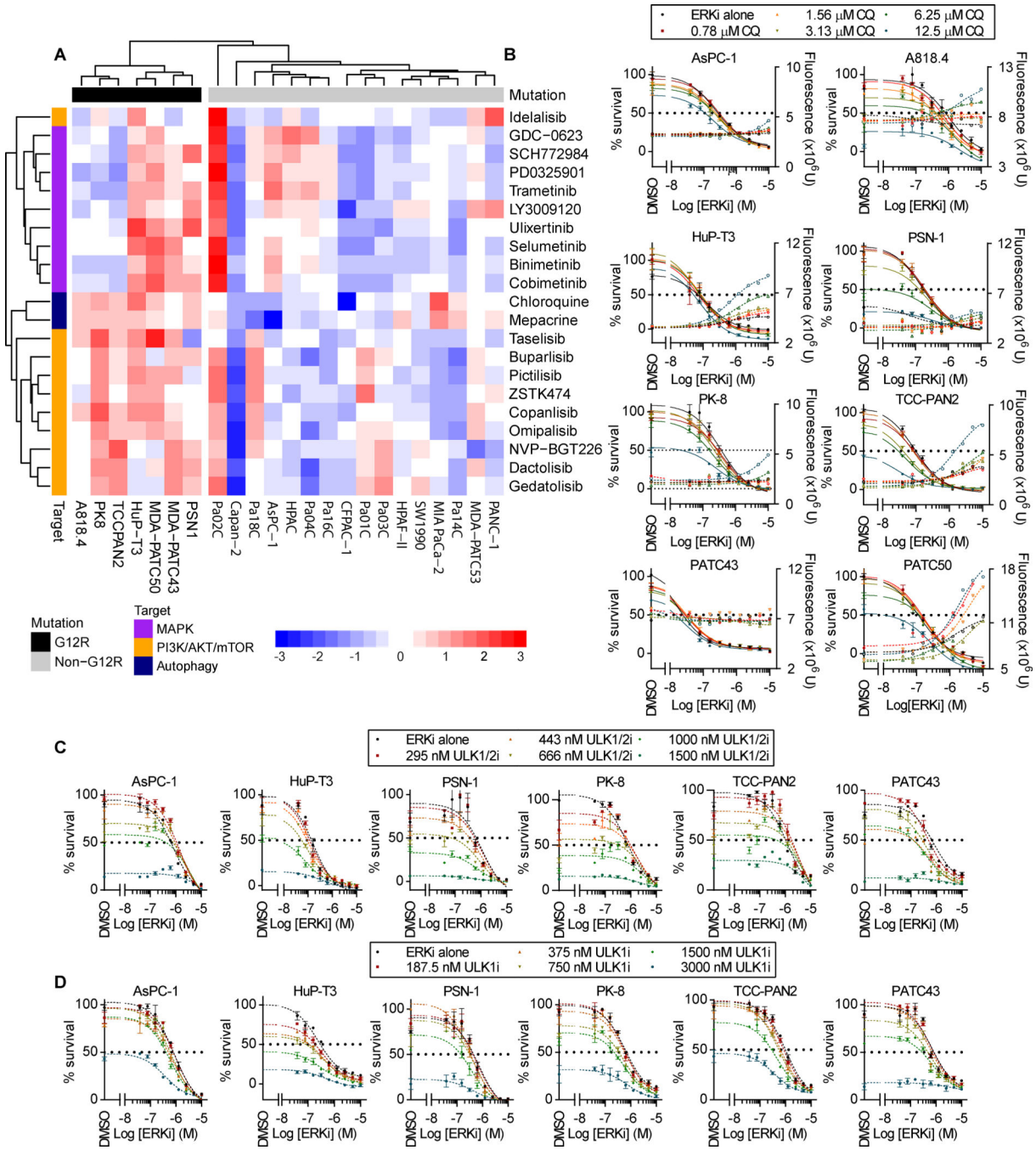

Figure 7.

KRAS^{G12R} PDAC are sensitive to inhibitors of autophagy. **A**, Heatmap from drug sensitivity and resistance testing of PDAC cell lines to >525 different inhibitors. KRAS^{G12R} cell lines showed increased sensitivity, relative to KRAS$^{G12D/V}$ cell lines, to inhibitors of ERK MAPK, PI3K and autophagy. **B**, Cell viability and cytotoxicity of select PDAC cell lines co-treated with SCH772984 (ERKi) and chloroquine (autophagy inhibitor, CQ). **C**, Cell viability of select PDAC cell lines co-treated with SCH772984 (ERKi) and the ULK inhibitor MRT68921 (MRT) after five days. **D**, Cell viability of select PDAC cell lines co-

treated with SCH772984 (ERKi) and the ULK inhibitor SBI0206965 (SBI) after five days. All data are representative of three independent experiments.